Norwegian University of
Science and Technology

Characterization of GaN:ZnO p-n junctions

Hege Knutsen

Master of Science in Physics and Mathematics
Submission date: June 2011
Supervisor: Ursula Gibson, IFY

Norwegian University of Science and Technology
Department of Physics

Abstract

In this master thesis, thin films of ZnO doped with various cobalt concentrations have been grown using Pulsed Laser Deposition (PLD). This growth technique is preferred because it is able to grow thin films from a target material without changing the elemental ratios from the target. The targets using during deposition are sintered pellets of ZnO doped with cobalt, with doping concentrations of 10, 20 and 30 %.

The material was chosen because of its potential for Intermediate Band Solar Cells (IBSC). IBSC is a new concept which aims to create solar cells which have higher efficiencies than the solar cells available today. From detailed balance theory, the concept of intermediate band solar cells shows a potential of a 86 % efficiency limit under perfect conditions, which is remarkable compared to the conventional silicon solar cell devices on the market today with a efficiency limit of 41 %.

A series of ZnO thin films of 10, 20 and 30 % cobalt concentration were deposited by PLD on a sapphire substrate. These films were, together with a similar series containing 1,2 and 5 % cobalt concentration deposited on both silicon and sapphire substrates, characterized using Scanning Electron Microscopy (SEM), Energy Dispersive X-ray (EDX) Microanalysis, X-ray Photoelectron Spectroscopy (XPS), Hall measurements, X-ray diffraction (XRD) and optical transmission spectroscopy.

In addition, an attempt to make Schottky diodes of the cobalt doped ZnO thin films and a p-IB-n junction using GaN:Mg and ZnO:Al as the p- and n- emitter was done. These intermediate band solar cell devices were going to be studied by recording dark and illuminated current-voltage (I-V) characteristics.

The focus in the study has been to determine which cobalt doping concentration gives the desired properties for use of ZnO:Co in an intermediate band solar cell device, and to study how a solar cell device with an intermediate band material can be realized. The experiments were carried out at NTNU NanoLab, NTNU Department of Physics, NTNU Department of Electronics and Telecommunications and SINTEF Oslo.

Optical transmission spectroscopy and XPS showed that the cobalt in the ZnO:Co films were Co^{2+}. This indicates that cobalt is substituting for zink in the ZnO lattice. XRD showed the crystal structure to be c-oriented with reasonable order. The carrier concentration in the ZnO:Co films were in the order of 10^{18}- 10^{19}, decreasing with increasing cobalt concentration. The resistivity in the samples increased with increasing doping concentration.

Investigation of the GaN:Mg wafer showed that it did not have the desired properties for device fabrication as it showed n-type conductivity instead of p-type. The Schottky diodes made of Au-ZnO:Co and Pt-ZnO:Co did not show diode behavior because of surface states in ZnO:Co making ohmic contacts.

Contents

Preface xi

1 Introduction **1**

2 Theory **5**

2.1 Basic concepts of solar cells 5
2.1.1 Semiconductor technology 5
2.1.2 The p-n junction 6
2.1.3 Fermi levels 6
2.1.4 Photon absorption 8
2.1.5 Loss mechanisms 8
2.1.6 The solar spectrum 9
2.1.7 Current - Voltage characteristics of the p-n junction . . 10
2.2 Detailed balance theory 13
2.3 Intermediate Band Solar Cells (IBSC) 16
2.3.1 Implementation of the IBSC concept 18
2.3.2 Detailed balance theory for IBSC 20
2.3.3 Metal-semiconductor (M-S) contacts 21
2.3.4 Properties of Schottky diodes 24
2.4 Hall effect and carrier concentration 25

3 Experimental techniques **29**

3.1 Pulsed Laser Deposition (PLD) 29
3.1.1 Light-material interaction 30
3.1.2 Film growth 31
3.2 Scanning Electron Microscopy (SEM) 31
3.3 Energy Dispersive X-ray (EDX) Microanalysis 32
3.4 X-ray Photoelectron Spectroscopy (XPS) 33
3.5 Optical transmission spectroscopy 34
3.6 X-ray Diffraction (XRD) 34

4 Background research **37**
4.1 ZnO:Co . . . 37
4.1.1 Pulsed Laser Deposition of ZnO, ZnO:Co and ZnO:Al . 38
4.1.2 Optical properties of ZnO:Co . . . 40
4.1.3 Electrical properties of ZnO:Co . . . 41
4.2 GaN:Mg . . . 42
4.2.1 Pre-treatments of Mg-doped GaN . . . 42
4.3 Ohmic contacts for GaN- and ZnO-devices . . . 44
4.4 Schottky contacts for ZnO-devices . . . 45

5 Equipment and Techniques **47**
5.1 Cleaning procedure for GaN:Mg wafers . . . 47
5.2 Activation of GaN:Mg . . . 47
5.3 Dry etch of GaN . . . 48
5.4 Pulsed Laser Deposition (PLD) of ZnO:Co high concentration samples . . . 48
5.5 Contact metalization of GaN:Mg and ZnO:Co . . . 49
5.5.1 Electron Beam Evaporator . . . 50
5.6 Hall measurements of GaN:Mg and ZnO:Co samples . . . 51
5.6.1 Additional I-V measurements of ZnO:Co Schottky diodes 52
5.7 Scanning Electron Microscopy (SEM) of GaN:Mg and ZnO:Co samples . . . 52
5.8 Energy Dispersive X-ray (EDX) analysis of GaN:Mg and ZnO:Co samples . . . 53
5.9 Optical Transmission Spectroscopy of ZnO:Co samples . . . 53
5.10 X-ray Photoelectron Spectroscopy (XPS) of ZnO:Co low concentration samples . . . 53
5.11 X-ray diffraction (XRD) of the ZnO:Co samples deposited on sapphire substrate . . . 54

6 Results and discussion **55**
6.1 GaN:Mg substrate treatments . . . 55
6.1.1 Etching characteristics for the GaN:Mg wafers . . . 56
6.2 Thickness measurements of the ZnO:Co thin films . . . 57
6.3 Dark I-V measurements to determine contact quality of the ZnO:Co and GaN:Mg semiconductor thin films . . . 58
6.4 Hall measurements to determine carrier concentration and resistivity estimates for the ZnO:Co thin films . . . 61
6.5 Optical properties of the ZnO:Co thin films . . . 63
6.6 Determination of the crystal-orientation in the ZnO:Co thin films . . . 69

6.7 Chemical composition 71
6.8 Device fabrication using ZnO:Co as intermediate band material 73

7 Conclusion and future work 77

A PLD parameters 79

List of Figures

1.1 Cost vs. efficiency for the three generation of solar cells. Figure is taken from [4] 3

2.1 Depletion region between a p-type and an n-type semiconductor. W is the width of the depletion region, ε is the electric field and qV_0 is the built in potential. Illustration based on illustration from [8]. 6

2.2 Energy of E_F as a function of the concentration of acceptors and donors. E_C and E_V are the energies of the conduction band and the valence band respectively. 7

2.3 Schematic of generation of electron-hole pair by an incoming photon with $E = h\nu > E_g$. 8

2.4 Extra-terrestrial (AM0) solar spectrum compared with 5760 K black body spectrum and with the standard terrestrial (AM1.5) spectrum. Illustration from [9]. 10

2.5 Energy band diagram of the p-n-junction with the work functions for the p- and n- type material, ϕ_p and ϕ_n, indicated. The illustration is based on illustration from [9]. 11

2.6 A p-n junction diode in the dark and when illuminated. The illustration is based on illustration from [4]. 12

2.7 Absorption and spontaneous emission. In figure a) a photon excites an electron to a higher energy state, while in figure b), spontaneous emission results in the emission of a photon. Illustration is based on illustration from [9]. 14

2.8 Band diagram illustrating the basic concepts that the intermediate band solar cell is based on. The CB, IB and VB represent the conduction band, intermediate band and valence band respectively, while E_{FC}, E_{FI} and E_{FV} are the quasi-Fermi levels for electrons in the three bands [6]. 17

2.9 Schematic of an IB sandwiched between an n and a p emitter. Illusration is based on illustration from [10]. 18

2.10 The positioning of the energy bands in an optimal IB structure 20
2.11 Typical measurements setup for contacts to a semiconductor. The current suffers voltage drops in the contact metal R_m, the contact junction R_c and in the semiconductor R_s. The current densiy j will be non-uniformly distributed. Illustration is based on illustration from [17]. 21
2.12 Energy band diagram for metal and p-type semiconductor in galvanic isolation. The essential parameters are included. Illustration based on illustration from [17]. 22
2.13 Schottky barrier for a metal/p-type semiconductor contact. Illustration based on illustration from [17]. 23
2.14 Schottky barrier for a metal/n-type semiconductor contact. Illustration based on illustration from [17]. 23
2.15 Illuminated characteristics of Schottky and p-n device. Illustration based on illustration from [4]. 25
2.16 Arrangement of the measurements of the Hall effect, showing the axes used. Illustration based on illustration from [19]. . . . 26

3.1 Physical processes involved in SEM imaging. Illustration from [21]. 32
3.2 Principles of EDX. Illustration is taken from [21]. 33

4.1 Hexagonal wurtzite structure of ZnO. The shaded gray and black spheres represents Zn and O atoms respectively. Illustration taken from [32]. 38
4.2 Carrier concentration at different temperature / time 44

5.1 Schematic diagram of the pulsed laser deposition experimental set-up. The illustration is based on illustration from [59] . . . 50
5.2 Contact configuration 51
5.3 Contact configuration for the Schottky contacts 51
5.4 Sample holder in the Hall measurement setup. 52
5.5 Diffractometer schematic. The illustration is based on illustration from [61]. 54

6.1 SEM surface pictures of the GaN:Mg wafer before and after etch 57
6.2 Cross section images of the a) 1 %, b) 2 % and c) 5 % Co sample. 58
6.3 IV curves recorded for the 1 % Co film for all the contact pairs 12, 23, 34 and 41 59
6.4 IV curves recorded for the GaN:Mg film activated at 580 ° C for all the contact pairs 12, 23, 34 and 41 60

6.5 Transmission spectra for the 1, 2 and 5 % cobalt doping concentration samples. 63
6.6 Transmission spectra for the 10, 20 and 30 % cobalt doping concentration samples. 63
6.7 Transmission spectra for the 1, 2, 5, 10, 20 and 30 % cobalt doping concentration samples. 64
6.8 Transmission spectra for the high concentration samples using the AvaSpec spectrometer. 65
6.9 Absorption coefficient as a function of cobalt doping concentration 66
6.10 Optical bandgap plots for Co-doped ZnO films 68
6.11 θ - 2θ curves for the high concentration samples. 70
6.12 Survey spectrum of the 2% Co sample deposited on silicon. . . 71
6.13 High resolution energy spectrum of the samples. 72
6.14 Dark I-V curves for M-ZnO:Co Schottky diodes 73
6.15 Dark I-V curves for Pt-ZnO:Co Schottky diodes for decreasing voltages 74
6.16 Possible circuit configurations for the M-ZnO:Co Schottky diodes. 74
6.17 Plot of the linear part of figure 6.15a for positive and negative voltages. 75

List of Tables

4.1 Overview of the different activation processes 44

5.1 Different recipes used in the RTP 48
5.2 Different recipes used in the ICP-RIE 49
5.3 Overview of samples deposited by PLD 50

6.1 Overview of the different pre-treatments with the resulting carrier concentration, type of charge carriers and resistivity estimates 56
6.2 EDX of a GaN:Mg sample before and after etching 57
6.3 Thickness measurements of the ZnO:Co samples on sapphire substrates 58
6.4 Resistivity estimates from Hall measurements 61
6.5 Resistivity estimates from four-point probe measurements . . . 61
6.6 Chemical composition of the samples on silicon from the XPS measurements. 72

A.1 Overview of samples deposited by PLD including all the parameters used 79

Preface

This master thesis is a result of my master work at Applied Physics at the Norwegian University of Science and Technology, Trondheim in the spring semester 2011. My supervisor has been Professor Ursula Gibson at Department of Physics.

The objective for this master thesis was to study the properties of GaN:ZnO p-n junctions. Since this turned out to be a challenge because our p-type material did not have the desired properties, the focus has changed somewhat during the semester into evaluating which cobalt doping concentration gives the desired properties for use of ZnO:Co in an intermediate band solar cell device, and to find out how a solar cell device with a ZnO:Co intermediate band can be realized.

I would like to thank my supervisor Professor Ursula Gibson for all the help she has given me during the semester, both in the lab and at her office. She has always been availiable for questions and proposed alternative solutions to unexpected propblems concerning the experimental work. I also appreciate her taking the time to read through my thesis during the semester.

I would like to thank Silje Rodahl at SINTEF Trondheim for helping me editing recipes for use in the Rapid Thermal Process Unit at NTNU NanoLab and showing me how use the Scriber/Breaker to properly cut the wafers used in this research. I would also like to thank master student Tor Ingve Aamot for his help and patience making X-ray diffraction measurements. I would like to thank Spyros Diplas for carrying out the X-ray photoelectron Spectroscopy experiment for me and the staff at NTNU NanoLab for always being of assistance. I would like to thank Cecile Ladam at SINTEF Trondheim for preparing the 1, 2 and 5 % Co concentration samples for me during the summer 2010.

Finally, I would like to thank Øystein Dahl at SINTEF Trondheim. He has taught me how to make thin film samples in a Pulsed Laser Deposition system, making Hall measurements, etching GaN samples and carrying out X-Ray Diffraction measurements. He has been available to help me in the lab when needed and together with my supervisor given me advices along the way to help me move forward.

Trondheim, June 2011 Hege Knutsen

Chapter 1

Introduction

The world's energy use increased more than ten times over the 20th century mainly from fossil fuels such as coal, oil and gas [1]. Because of the rising industrialization and demand in previously less developed countries the increase in world energy consumption will increase further in the 21st century and the need for efficient generation and use of energy is evident.

Fossil fuels is a limited resource, and the latest survey suggest that the lifetime of these resources is only a few decades for oil and gas, and a few centuries for coal [1]. Also, the environmental effects of burning fossil fuels imply that CO_2 emission from the combustion have raised the concentration of CO_2 in the atmosphere. This will over time enhance the greenhouse effect and lead to significant climate change within a century or less [1]. This may be the main reason why renewable energy resources have been gaining increasing interest in national energy planning. In 2008, renewable energy technologies accounted for 19 % of the global electricity generation [2]. Hydropower is the most important renewable energy source (16 %), while the last 3 % includes geothermal, solar, wind, combustible renewables and waste, and heat.

Photovoltaic conversion of solar energy is a clean way of producing electrical energy [3]. The concept was first discovered in 1839 by Alexandre-Edmond Becquerel. He observed a light-dependent voltage between electrodes immersed in an electrolyte [4]. In 1876, this effect was observed in an all-solid-state system. In 1954, a forerunner of present silicon cells was announced. This was the first photovoltaic structure that converted light to electricity with reasonable efficiency [4]. Since the 1970's, photovoltaic power has been one of the fastest growing renewable energy technologies [1]. The advantages of photovoltaics are many including modular character, stand-alone and grid-linked opportunities, reliability, ease of use, lack of noise and emission and reducing costs per unit energy produced [1].

Today much of the research in solar cell technology is concerned with improving the conversion factor of the solar cells and reducing the costs to make it economically competitive. Silicon has up to now been the leading material because it is non-toxic and highly abundant. Its band gap of 1.1 eV covers 2/3 of the solar spectrum [1] and makes it desirable for solar cells. The extended research of this material has made it possible to produce solar cells with an efficiency approaching the theoretical limit of 41 % under direct illumination [1]. The major drawback of silicon solar cells is the large amount of energy required in the production of high-quality silicon [5].

Silicon wafer-based solar cells are first generation solar cells. Second generation solar cells are made of cheaper materials, normally in the form of thin films such of Si, CdTe, $CuInGaSe_2$ or Grätzel-cells which are dyes in a porous nanocrystalline TiO_2 [1]. The disadvantage of this generation of solar cells is that the efficiencies are low [1]. Both first and second generation solar cells are single junction cells and the efficiency limit is 31 % for unconcentrated solar radiation, and 41 % for full concentration [1].

To make solar cells with higher efficiencies, new materials and concepts for solar cells devices are being exploited. Third generation solar cells try to combine high efficiencies with low cost compared to the first and seconds generation solar cells [1]. The strategies for third generation solar cells are to utilize more of the solar spectrum, to increase the work per photon by utilizing some of the excess kinetic energy of the photogenerated carriers before they relax or to increase the number of electron-hole pairs per photon. Various new concepts are introduced, such as hot-carrier cells, multiple charge carriers per absorbed photon by impact ionization, tandem cells and intermediate band cells based on multiple band gaps [6].

The concept of intermediate band solar cells (IBSC) was first introduced by Luque and Marti in 1997. They presented a model of an ideal solar cell with an intermediate energy band within the semiconductor band gap [7]. This structure allows for two-step absorption of sub-band photons without reducing the output voltage. In this way, photons with energies lower than the band gap may be absorbed and contribute to the total efficiency of the cell. The theoretical limit for IBSC with one intermediate band (IB) is 63.2 % under full illumination. With an infinite number of sub-gaps its limiting efficiency is 86.8 %, the same as that of a stack with an infinite number of single-gap solar cells [6]. Since the concept was introduced, both theoretical studies and practical efforts have been carried out that aim to manufacture prototypes of IBSC [6]. At present, three different approaches are being carried out to manufacture an IBSC. These are the direct synthesis of a material with an IB, the so-called highly nanoporous material approach and its implementation by means of quantum dots (QD) [6].

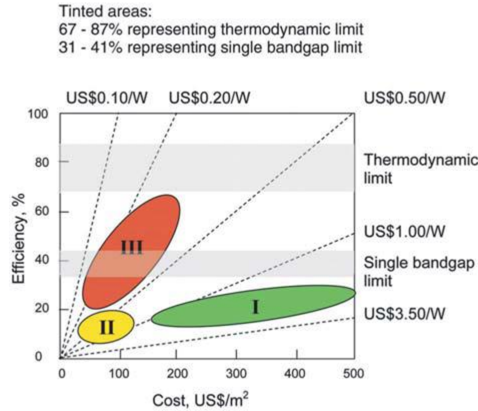

Figure 1.1: Cost vs. efficiency for the three generation of solar cells. Figure is taken from [4]

In this thesis, ZnO doped with cobalt were investigated as a possible material for intermediate band solar cells. Pulsed Laser Deposition (PLD) was used to make thin films of ZnO:Co with various doping concentrations. The thin films were investigated in detail by Scanning Electron Microscopy (SEM), X-ray Photoelectron Spectroscopy (XPS), Energy Dispersive X-ray (EDX), X-ray diffraction (XRD), Hall measurements and optical transmission spectroscopy. The focus in this master thesis was to determine how the various cobalt concentrations influenced the electric and optical properties in the thin films of ZnO:Co and to investigate the possibilities for using this material in an intermediate band solar cell device.

Chapter 2 contains the relevant theory including basic concepts of solar cells and detailed balance theory. In addition, the theory for IBSC is explained in detail. The experimental techniques used are explained in chapter 3. In chapter 4, a summary of previous work is presented. This chapter includes previous research on the materials used in this thesis, including deposition techniques and characterization of electric and optical properties of the materials. Chapter 5 gives an overview of the work done in the lab and how the different samples were deposited and characterized. Chapter 6 contains the result of the measurement together with discussion of the different results. A conclusion of the work is given in chapter 7. This chapter also includes proposed future work to continue the research presented in this thesis.

Chapter 2

Theory

In this chapter, the relevant theory is being presented. The first part includes the basic concept of a standard solar cell based on a semiconductor material. Section 2.2 explains the concept of detailed balance and includes detailed balance calculations for the standard solar cell. The intermediate band solar cell is being presented in section 2.3 and includes detailed balance calculations for this configuration. The last part of this chapter includes concepts of metal-semiconductor contact configurations and the Hall effect.

2.1 Basic concepts of solar cells

2.1.1 Semiconductor technology

A semiconductor is a material with a narrow forbidden band gap. This means that at low temperatures, it doesn't conduct any current and all the electrons are in the lower valence band and the conduction band is empty. As the temperature increase, the kinetic energy of the electrons makes it possible that some cross the energy gap between the valence and the conduction band; electrons in the valence band are thermally excited to the conduction band leaving holes in the valence band. In an intrinsic semiconductor (without any defects or impurities), the number of electrons and holes are equal [4]

$$n = p = p_i \tag{2.1}$$

where i means intrinsic. Current flow in semiconductors is due to both motion of electrons in the conduction band and holes in the valance band [4].

2.1.2 The p-n junction

Doping the semiconductor with donor impurities gives an increased number of electrons in the conduction band at normal temperatures and is known as n-type material. This means that the number of electrons in the conduction band n_0 is much greater than n_i for normal doping levels. Similarly, when doping with acceptor impurities, p-type material is obtained. When the n-type and the p-type material are brought together, excess donor electrons from the n-type material cross to the acceptor p-type material and vice versa for holes. A steady state is reached when the electric field caused by the accumulated charge carriers on each side of the junction balances the diffusive force arising from the different concentrations of free electrons and holes [1]. The transition region between the n-type and the p-type semiconductors is called the space-charge region [8] or depletion region [8]. A figure of the depletion region between a p-type and an n-type semiconductor i shown in figure 2.1

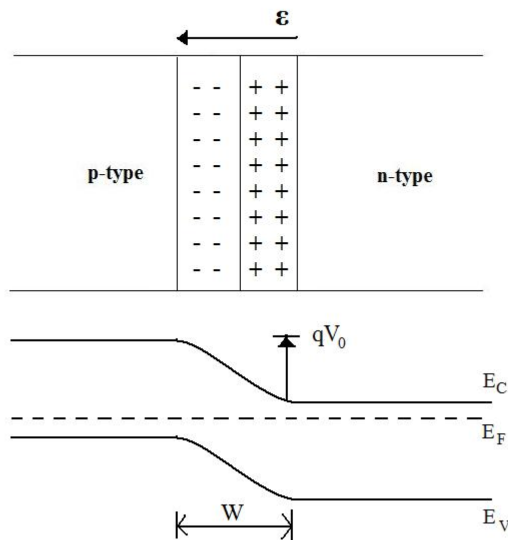

Figure 2.1: Depletion region between a p-type and an n-type semiconductor. W is the width of the depletion region, ε is the electric field and qV_0 is the built in potential. Illustration based on illustration from [8].

2.1.3 Fermi levels

The Fermi level is defined as the energy level up to which all available states in the crystal are occupied at zero temperature [4]. As the temperature

increases, some electrons gain energy in excess of the Fermi level. The probability of occupation of an allowed electron state of any given energy E can be calculated from statistical considerations [4]. The result is the Fermi-Dirac distribution *f(E)*, given by

$$f(E) = \frac{1}{1 + e^{(E-E_F)/kT}} \tag{2.2}$$

Close to absolute zero, *f(E)* is approximately unity until the energy E is equal to E_F. Above this energy level the value of *f(E)* is zero. As the temperature rises, the distribution smears out with states of energy higher that E_F having a finite probability.

In an intrinsic semiconductors, the number of electrons in the conduction band equals the number of holes in the valence band so the Fermi energy lies very close to the middle of the band gap [8]. The carrier concentration is typically very small for intrinsic semiconductors and they behave much like insulators [8].

Dopants introduce additional localized electronic states into the band structure often within the forbidden gap between the valence band and the conduction band [8]. In n-type material, donor atoms introduce an energy state close to the conduction band edge, and the Fermi level will move up towards the band edge of the conduction band. Similarly, in p-type material the Fermi level will move towards the edge of the valence band. This is shown schematically in figure 2.2.

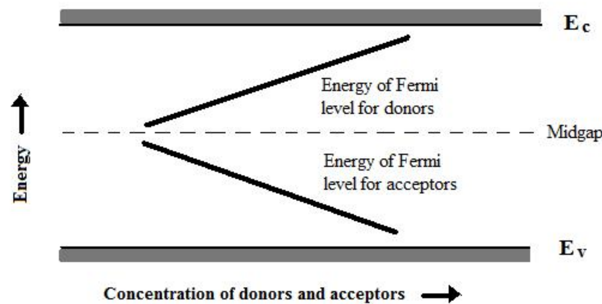

Figure 2.2: Energy of E_F as a function of the concentration of acceptors and donors. E_C and E_V are the energies of the conduction band and the valence band respectively.

On the energy scale, the Fermi level of the n- and p-type semiconductor will fall together in thermal equilibrium and we will get an energy difference

between the valence band and the conduction band. In figure 2.1 the energy band diagram including the Fermi level of the p-n junction at thermal equilibrium is illustrated.

Under illumination, the cell is no longer in thermal equilibrium, so the Fermi level for the system is replaced by quasi-Fermi levels of the n- and p-type semiconductor [9].

2.1.4 Photon absorption

A photon with energy $E = h\nu > E_g$ may be absorbed within the p-n-junction and create an electron-hole pair when an electron is excited from the valence band to the conduction band. The free charge carriers generated will be separated by the built-in electric field at the p-n junction if they are generated close enough to it, i.e. within a diffusion length from the junction [1] . The absorption process is illustrated in figure 2.3. Here, the Fermi level has been replaced by the quasi-Fermi levels E_{Fn} and E_{Fp} of the n- and p-type semiconductor respectively.

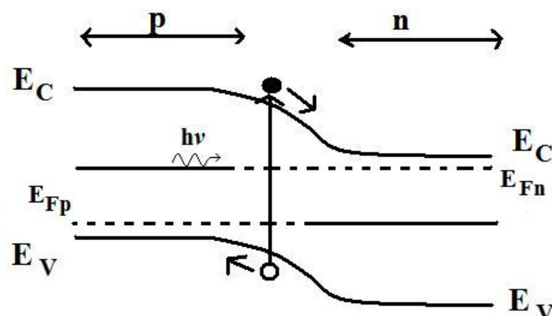

Figure 2.3: Schematic of generation of electron-hole pair by an incoming photon with $E = h\nu > E_g$.

Connecting the solar cell to a resistance load, the exited charge carriers will diffuse to the external circuit.

2.1.5 Loss mechanisms

There are several mechanisms that contribute to the decrease in efficiency of the solar cell. The two most important is that photons with energy $h\nu < E_g$ cannot contribute to photovoltaic current generation (23 % energy loss), and the excess energy of photons with $h\nu > E_g$ will result in heating of the semiconductor (33 % energy loss) [1]. Also, the energy of the photoelectrically exited charge carriers is not equal to the band gap of the semiconductor, but

determined by the band potential V_0 across the junction in open circuit (20 % energy loss) [1]. Recombination of generated electron and hole carriers inside the semiconductor will also reduce the efficiency of the solar cell as the charge carriers do not reach the external circuit (4 % energy loss). Radiative recombination involves direct carrier transitions to the valence band and the resulting emission of radiation while non-radiative recombination centers comes from impurities and crystal defects [1].

2.1.6 The solar spectrum

The energy delivered from a solar cell is dependent on the incident solar spectrum. For theoretical calculations, the spectrum from the sun is often consider to be a black-body with a surface temperature of 5760 K, because this spectrum resembles the spectrum from the sun, which has a surface temperature of 5760 K, and can be described by analytic mathematical functions. A black body emits photons with a distribution of energies determined by its characteristic temperature, T_s [9]. At a point s on the surface, the black body emits a number of photons with energy in the range of E to $E + \delta E$ through a unit area per unit solid angle per unit time. This *spectral photon flux*, $\beta_s(E, s, \theta, \phi)$ is given by

$$\beta_s(E, s, \theta, \phi) d\Omega d\boldsymbol{S} dE = \frac{2}{h^3 c^2} \left(\frac{E^2}{e^{\frac{E}{k_B T_s}} - 1} \right) d\Omega d\boldsymbol{S} dE \qquad (2.3)$$

where $d\boldsymbol{S}$ is the element of surface area around s and $d\Omega$ is the unit of solid angle around the direction of emission of the light (θ, ϕ)

In figure 2.4, the black-body spectrum at 5760 K is compared to the AM0 and AM1.5 spectrum. The AM0 and AM1.5 stands for "air mass " 0 and 1.5 and refers to the spectrum of the sunlight outside the atmosphere and the solar spectrum after it has passed through air corresponding to 1.5 times the thickness of a standardized atmosphere of the earth respectively [5]. The terrestrial spectrum (AM1.5) describes the light that actually reaches the Earth's surface after passing through the atmosphere. There are various wavelengths in which the number of photons is greatly reduced as compared to the space solar spectrum due to photons being absorbed by atmospheric gases such as ozone (O_3) and water vapor (H_2O).

Solar cells without concentration systems will receive radiation scattered from the surroundings in addition to the radiation coming directly from the sun [5]. For a concentrating solar cell device, the scattered light will make a very small contribution compared to the direct light, so two different version of the AM1.5 are being used. This is the AM1.5D, where D stands for direct,

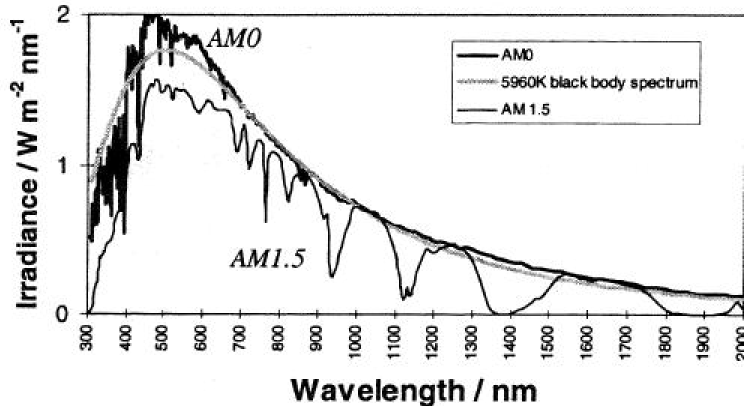

Figure 2.4: Extra-terrestrial (AM0) solar spectrum compared with 5760 K black body spectrum and with the standard terrestrial (AM1.5) spectrum. Illustration from [9].

which is used for the spectrum ignoring the scattered light, and the AM1.5G, where G stand for global, where the scattered light is taken into account [5].

2.1.7 Current - Voltage characteristics of the p-n junction

To analyze the current-voltage characteristics of the p-n junction, it is common to use the *depletion approximation* for the p-n junction device. This approximation divides the device into two types of regions; the quasi neutral-region and the depletion region. In the quasi-neutral region, the space-charge density is assumed zero, while in the depletion region the carrier concentrations are assumed so small that the only contribution to space charge density comes from ionized dopants [4]. This means that there is a sharp transition between the space charge region and the p- and n-type semiconductor respectively. When in addition assuming that the recombination is linear throughout the device, analytic functions for the current density $J(V)$ can be derived for different conditions [9].

The built in potential over the p-n junction in thermal conditions, V_0, is determined by the difference in work functions for the p- and n- type material, ϕ_p and ϕ_n [9]. This difference is equal to the shift of Fermi levels from the intrinsic potential energy (E_i) of the semiconductor since E_i is parallel to E_{vac}.

This means that the potential V_0 is equal to

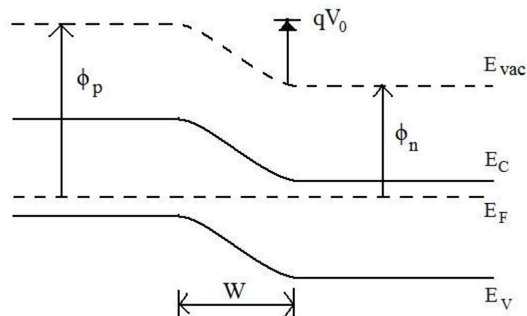

Figure 2.5: Energy band diagram of the p-n-junction with the work functions for the p- and n- type material, ϕ_p and ϕ_n, indicated. The illustration is based on illustration from [9].

$$V_0 = \frac{1}{q}(\phi_p - \phi_n) \tag{2.4}$$

If an external electrical bias is applied over the p-n junction, it raises the Fermi level of one side with the respect to the other and the potential drop across the junction becomes [9]

$$V_j = V_0 - V \tag{2.5}$$

where V is the bias applied to the p-side. A negative applied bias will draw carriers from the junction region increasing the depletion region while a positive bias will inject carriers and reduce the depletion region. Illumination of the p-n junction will shift the Fermi level in the same way as a positive applied bias since photogenerated holes will build up on the p-side and electrons on the n-side [9].

The current density $J(V)$ in the p-n junction is zero under equilibrium conditions in the dark [9]. Under forward bias, the current density is given as

$$J_{dark} = J_0(e^{qV/mkT} - 1) \tag{2.6}$$

where J_0 is a constant and m is the ideality factor. The dark current includes radiative recombination J_{rad}, diffusion J_{diff} and recombination in

the space charge region J_{SCR} interpreted in the ideality factor. For an ideal diode, m =1.

Under illumination, light creates electron-hole pairs and the quasi-Fermi level of the p-n junction is split as explained in section 2.1.4. In this situation, the current density is dependent on both the short-circuit photocurrent I_{sc} and the dark current at that bias $J_{dark}(V)$ [9]. The short circuit photocurrent can be calculated using $V = 0$, that is the quasi-Fermi level in the space-charge region is the same on both the p- and n-side [9]. This result in a current-voltage characteristic given as

$$J(V) = J_{SC} - J_{dark}(V) = J_{SC} - J_{m,0}(e^{qV/mkT} - 1) \tag{2.7}$$

Figure 2.6 shows the properties of a p-n junction diode (m=1) in the dark and when illuminated. The illuminated characteristics is approximately the dark characteristics shifted down by a current I_{SC}.

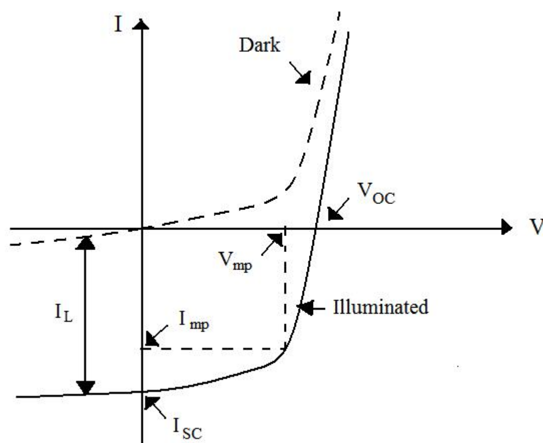

Figure 2.6: A p-n junction diode in the dark and when illuminated. The illustration is based on illustration from [4].

To find the open circuit voltage, that is when no current is drawn from the circuit, setting $J(V)$ to zero and rearranging equation (2.7) gives

$$V_{OC} = \frac{mkT}{q} ln\left(\frac{J_{SC}}{J_{m,0}} + 1\right) \tag{2.8}$$

V_{OC} is determined by the properties of the semiconductor by its dependence on I_0.

The fill factor FF is often used to characterize the performance of a solar cell device [4]. It is defined as

$$FF = \frac{V_{mp} I_{mp}}{V_{OC} I_{SC}} \tag{2.9}$$

where V_{mp}, I_{mp} is one particular operating point which maximizes the power output of the device. It defines how "square" the output characteristics are and has the value in the range 0.7 to 0.85 for cells of reasonably efficiency [4].

2.2 Detailed balance theory

Detailed balance is often used to calculate the limiting efficiencies of solar cell devices. The theory takes into account several assumptions about the physical system when setting up the calculations. The assumptions rely on a perfect photovoltaic structure, and they are summarized in [9] as follows:

- The photovoltaic material has an energy gap which separates states which are normally full from states which are normally empty
- All incident light with E > E_g is absorbed
- Each absorbed photon generates exactly one electron-hole pair
- Excited charges do not recombine except radiatively
- Excited charges are completely separated
- Charges is transported to the external circuit without loss

In the dark, the solar cell is in equilibrium with its ambient. Assuming that the ambient radiates like a black body with temperature T_a, the spectral photon flux at a given point s on the solar cell is given according to equation (2.3) as

$$\beta_a(E, s, \theta, \phi) d\Omega d\boldsymbol{S} dE = \frac{2}{h^3 c^2} \left(\frac{E^2}{e^{\frac{E}{k_B T_a}} - 1} \right) d\Omega d\boldsymbol{S} dE \tag{2.10}$$

To obtain the incident flux of thermal photons normal to the surface of a flat planar solar cell, $\beta_a(E, s, \theta, \phi)$ is integrated over all directions, and the result is

$$b_a(E) = \frac{2F_a}{h^3 c^2} \left(\frac{E^2}{e^{\frac{E}{k_B T_a}} - 1} \right) d\Omega d\boldsymbol{S} dE \tag{2.11}$$

where F_a is a geometrical factor $=\pi$ is the ambient radiation is received over a hemisphere [9].

The equivalent current density absorbed from the ambient is given by

$$j_{abs}(E) = q(1 - R(E))a(E)b_a(E) \tag{2.12}$$

where $a(E)$ is the probability of absorption of a photon with energy E and $R(E)$ is the probability of photon reflection [9]. $a(E)$ is dependent on the absorption coefficient of the material and the optical path length through the device.

The cell emits photons by spontaneous emission, and in thermal equilibrium, this radiation is given by

$$j_{rad}(E) = q(1 - R(E))\epsilon(E)b_a(E) \tag{2.13}$$

where $\epsilon(E)$ is the emissivity.

In detailed balance, the two current densities given in equation 2.12 and 2.13 must be equal, which means that

$$a(E) = \epsilon(E) \tag{2.14}$$

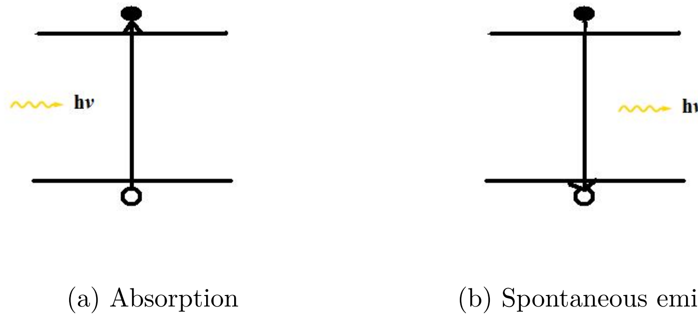

(a) Absorption (b) Spontaneous emission

Figure 2.7: Absorption and spontaneous emission. In figure a) a photon excites an electron to a higher energy state, while in figure b), spontaneous emission results in the emission of a photon. Illustration is based on illustration from [9].

Under illumination

When the solar cell is under illumination of a solar photon flux β_s(equation (2.12)) the cell absorbs solar photons with energy E at a rate of

$$(1 - R(E))a(E)b_s(E) \tag{2.15}$$

The equivalent current density for photon absorption includes a contribution from thermal photons in addition to solar photons,

$$j_{abs}(E) = q(1 - R(E))a(E)\left(b_s(E) + \left(1 - \frac{F_s}{F_e}\right)b_a(E)\right) \tag{2.16}$$

Under illumination, part of the electron population has increased electrochemical potential energy and the system develops a net chemical potential $\Delta\mu > 0$. The rate of emission depends on $\Delta\mu$ as more exited electrons leads to higher frequency of relaxation. According to Planck's law of radiation, the spectral photon flux when a chemical potential is introduced is given by

$$\beta(E, s, \theta, \phi) = \frac{2n_s^2}{h^3c^2}\left(\frac{E^2}{e^{\frac{E-\Delta\mu}{k_BT_a}} - 1}\right) \tag{2.17}$$

per unit and solid angle. n_s is the refractive index of the cell material. To obtain the photon flux emitted normal to the surface, an integration is taken over the range of solid angle where photons can escape. When in addition assuming air as the surrounding medium and a planar solar cell, the integration leads to a photon flux

$$b_e(E, \Delta\mu) = \frac{2\pi}{h^3c^2}\left(\frac{E^2}{e^{\frac{E-\Delta\mu}{k_BT_a}} - 1}\right) \tag{2.18}$$

The equivalent current density for photon emission is

$$j_{rad}(E) = q(1 - R(E))\varepsilon(E)b_e(E, \Delta\mu) \tag{2.19}$$

When the cell is in equilibrium, this equation reduces to equation 2.13 as $\Delta\mu = 0$ and $a = \epsilon$. With $\Delta\mu > 0$ under illumination, it's is not straight forward to see how $a(E)$ relates to $\epsilon(E)$ but it can be shown that if $\Delta\mu$ is constant through the device, equation 2.14 still holds [9].

The result is a net current density given from equation 2.19 and 2.16 as

$$j_{abs}(E) - j_{rad}(E) = q(1 - R(E))a(E)\left(b_s(E) + \left(1 + \frac{F_s}{F_a}\right)b_a(E) - b_e(E, \Delta\mu)\right) \tag{2.20}$$

The net current density can be divided into a net absorption part

$$j_{abs(net)}(E) = q(1 - R(E))a(E)\left(b_s(E) - \frac{F_s}{F_e}b_a(E)\right) \tag{2.21}$$

and a net radiation part

$$j_{rad(net)}(E) = q(1 - R(E))a(E)(b_e(E, \Delta\mu) - b_e(E, 0)) \tag{2.22}$$

Here, $b_a = b_e(E, 0)$

The net radiative current density is known as radiative recombination and is unavoidable loss, which means that all absorbed solar radiant energy cannot be utilized by the solar cell.

When calculation efficiency limits, the absoptivity for a specific photon energy should be either 0 or 1 [5]. The absorptivity is 0 for photons with energy lower than the band gap. It should also be 0 for photon energies where the number of emitted photons exceeds the number of absorbed photons. However, the usual way to calculating the total efficiency is to assume that the absorptivity is unity for all photons above the band gap energy [5].

2.3 Intermediate Band Solar Cells (IBSC)

IBSC are based on the p-n junction as in the ordinary semiconductor solar cells. The main difference is that you introduce several band gaps to collect the radiation from the sun more efficiently. Figure 2.8 shows a band diagram for a material with an intermediate band in the forbidden band gap of the semiconductor. The intermediate band (IB) allows for the absorption of sub-band gap photons such as those labeled (1) and (2). Photon (1), with energy $E_1 < E_g$ is absorbed and an electron is excited from the valence band to the intermediate band. Then, a second electron with energy $E_2 < E_g$ is absorbed and the electron in the intermediate band is excited to the conduction band. In addition, photons with energy $E_3 > E_g$ excite an electron directly from the valence band to the conduction band.

As described in section 2.1.5, non-radiative losses reduce the efficiency of the solar cell. When introducing deep level impurities with discrete energy levels within the bandgap, as usually occurs in conventional solar cells, non-radiative recombination centers will be formed [6]. The mechanism for the non-radiative recombination centers can be explained by considering a transition of an electron from the conduction band to a localized impurity state in the band gap. The charge of the electron which was formerly distributed across the whole crystal becomes closely packed around the impurity. This causes the impurity to be out of equilibrium, and surrounding atoms will start to vibrate to find a new equilibrium. The vibration is eventually damped by

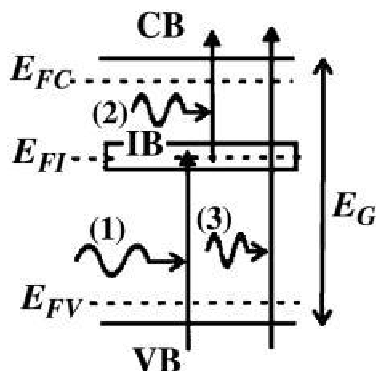

Figure 2.8: Band diagram illustrating the basic concepts that the intermediate band solar cell is based on. The CB, IB and VB represent the conduction band, intermediate band and valence band respectively, while E_{FC}, E_{FI} and E_{FV} are the quasi-Fermi levels for electrons in the three bands [6].

phonon-phonon or phonon-electron interactions to thermal equilibrium [3]. A second transition from the impurity to the valence band will again cause the impurity to be out of equilibrium, and the vibrations will eventually be damped. The reason why the transition from the CB to the impurity occurs is that when the impurity is in a non-equilibrium position, the energy level of the filled trap is situated at an energy similar or close to the conduction band [3]. Similarly, a transition from the impurity to the valence band occurs when the energy of the filled trap is close to the energy of the valence band.

Increasing the density of impurities will cause the electron wave functions in these intermediate states not to be localized anymore and become extended to the whole volume of the material [6]. In this way, a transition from the CB to the impurity band will not involve a large charge movement and disequilibrium [3]. This causes the radiative recombination to exceed the non-radiative one [6]. As radiative recombination becomes dominant, the recombination lifetimes between the three bands is expected to be much larger than the carrier relaxation times in each of the bands [6].

The carrier concentration in each of the bands are described by its own quasi Fermi level, E_{FC}, E_{FI} and E_{FV}. To be able to accommodate both electrons coming up from the valence band and to supply electrons to be pumped into the conduction band it is necessary for the IB to be half-filled with electrons. This requires the IB quasi-Fermi level, E_{FI}, to be within the IB [6].

A realization of the intermediate band solar cell is to introduce the intermediate band material between an n-type and a p-type semiconductor emitter. In this way, a so-called p-IB-n junction is formed. Figure shows a schematic of an IB sandwiched between an n and a p emitter

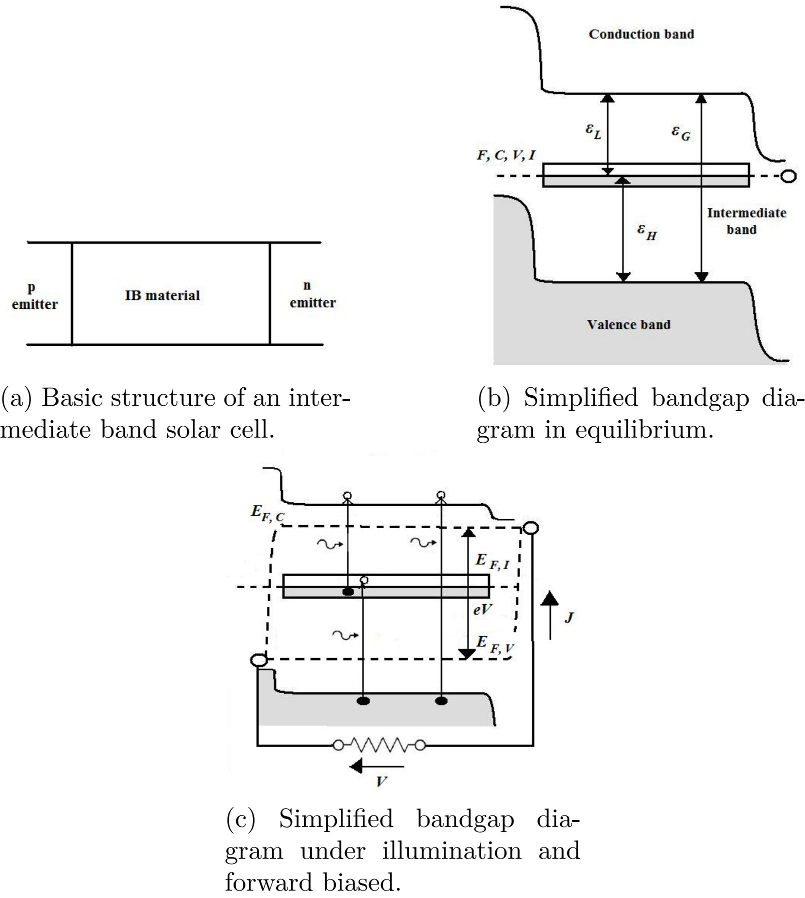

(a) Basic structure of an intermediate band solar cell.

(b) Simplified bandgap diagram in equilibrium.

(c) Simplified bandgap diagram under illumination and forward biased.

Figure 2.9: Schematic of an IB sandwiched between an n and a p emitter. Illusration is based on illustration from [10].

The n- and p-type emitter are present to separate the electron and holes generated in the intermediate band region.

2.3.1 Implementation of the IBSC concept

There are three different approaches being carried out to manufacture an IBSC. These are the direct synthesis of a material with an IB, the so-called highly nanoporous material approach and its implementation by means of

quantum dots (QD) [6]. The work done in this thesis is the direct synthesis approach.

The first concept proposed was the use of quantum dot superlattices [5]. A quantum dot (QD) is a small particle (nm-scale) of a particular material. Quantum mechanical effects will introduce discrete energy levels in particles with this size [5]. When many quantum dots are closely spaced, the electron wavefunction will become delocalized and an intermediate band is formed. Attempts including using III-V semiconductors have been carried out, but the efficiencies of the cells have not been higher than the reference cell without the QDs. The concept of two-step photogenerated process have however been observed as photons with energies lower than the band gap have been absorbed in the cell, causing increased photocurrent in the cell [11].

Molecular intermediate band solar cell is a new concept, where organic molecules complexing metal atoms are used [5]. The long lifetime of excited triplet states (typically hundreds of microseconds in solution at room temperature) in molecular materials offers a unique opportunity to store energy in a photovoltaic device [12]. The limiting efficiency for this system exceeds that of a single bandgap device, peaking at 40.6% for 1.9 eV under 1 sun illumination [12].

The last concept proposed is the direct synthesis of a material with an IB. Initially, the question was whether a material with a half-filled IB could exist or not [6]. Crystalline structures and different atomic species were studied to find out which structures could lead to a band diagram having the required IB. One type of materials studied is crystalline lattice of several III-V compound semiconductors by means of the insertion of transition atoms into the lattice at the correct sites [6]. If the transition atoms can be incorporated into the semiconductor host at a sufficiently high density, an IB can arise from deep centers within the semiconductor bandgap [13]. Studies of Ga_4P_3Ti in terms of density of states, electronic density, and atomic and orbital populations [14] have shown that an isolated half-filled intermediate band that can absorb low-energy photons exists in this material. In [15] *ab inito* calculation showed an intermediate narrow band formed between the valence band and the conduction band in compounds of Ga_4As_3Ti and Ga_4P_3Ti. The intermediate band in these material is related to the valence band by a direct transition band gap and with the conduction band by an indirect transition band gap. Oxygen doping in ZnTe has also been investigated for IB material [16]. In the research, diodes made from ZnTe:O showed extended spectral response below the bandedge relative to undoped ZnTe diodes and the overall power conversion efficiency was 50 % greater than for the undoped material. The subbandgap excitations related to oxygen doping was dominated by defect emission in the range from 1.6 -2.0 eV, while the bandgap excitation

energy was ~2.3 eV for both the undoped ZnTe and ZnTe:O diodes [16].

2.3.2 Detailed balance theory for IBSC

The detailed balance theory can be applied to intermediate band solar cells with some adjustments. The important thing to consider is that three recombination routes and three generation routes exist. The idealities assumed in addition to the ones mentioned in section 2.2 is that the width of the intermediate band, $\Delta \boldsymbol{E}$ is zero and that the material with the IB has non-overlapping absorption coefficients [5]. Non-overlapping absorption coefficients means that for a given photon energy only one absorption process is possible. For a given photon energy, the absorption coefficient should be zero for excitations over all band gaps except the highest possible band gap [5].

The net current density is still given by equations (2.20), (2.21) and (2.22), but three different contributions with non-overlapping absorption coefficients exist i.e. for absorption from the valence band to the intermediate band, from the intermediate band to the conduction band and from the valence band to the conduction band.

In [7] calculations on the optimum positioning of the intermediate band based on detailed balance have been made. For a solar cell with one intermediate band, the highest efficiency of 63.2 % is obtained when the total band gap of the material is 1.95 eV, with an intermediate band positioned 1.24 eV above the valence band. An illustration of this configuration is shown in figure 2.10, where the intermediate band is half-filled, which is one of the assumptions for the detailed balance calculations performed.

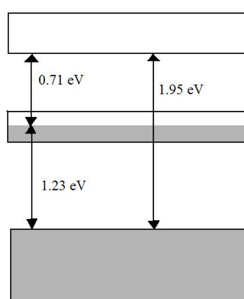

Figure 2.10: The positioning of the energy bands in an optimal IB structure

2.3.3 Metal-semiconductor (M-S) contacts

The theory in this section are a summary of chapter 2.2 and 2.3 in [17]. The fabrication of good ohmic contacts to a semiconductor device is important to be able to connect the semiconductor electrically to other devices. In this work, contacts to GaN:Mg and ZnO:Co were made to be able to measure electrical properties of the thin films and eventually be able to connect the solar cells to other devices. Ohmic behavior is often interpreted as linear I-V characteristics [17]. For a semiconductor device, this characterization is not sufficient as large series resistance will degrade the operation of a semiconductor device. Ohmic contact is understood as a contact that does not influence the device performance [17].

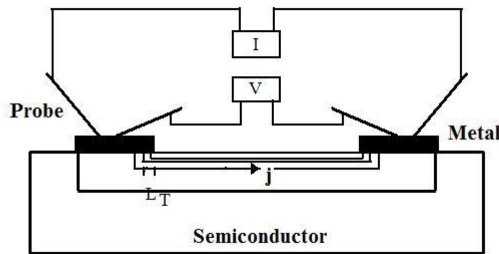

(a) Sketch of typical measurements situation for contacts to a semiconductor.

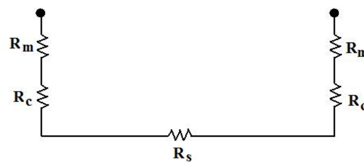

(b) Series resistance in measurement setup.

Figure 2.11: Typical measurements setup for contacts to a semiconductor. The current suffers voltage drops in the contact metal R_m, the contact junction R_c and in the semiconductor R_s. The current densiy j will be non-uniformly distributed. Illustration is based on illustration from [17].

Figure 2.11 shows a typical setup for measuring contact resistance. With a linear, low resistivity contact, the total measured resistance may be found by a linear fit to the I-V curve recorded when passing a current from one contact to the other and measuring the voltage. If the contacts are assumed to be identical, the total resistance is given by

$$R_T = 2R_c + 2R_m + R_s \tag{2.23}$$

In most cases, the metal resistance R_m is considered to be zero, while the contact resistance R_c is dependent on the size and geometry of the contacts. The current flow will not be uniformly distributed across the contacts, but passes through a small part of the contact to minimize the total resistance [17].

To analyze the electronic transport properties of metal-semiconductor (M-S) contacts, some essential parameters are needed for the analysis. In figure 2.12, the energy band diagram for a M-S contact in galvanic isolation is illustrated. According to principles of energy and charge conservation, the Fermi level of the metal and the semiconductor will align at equilibrium. The alignment occurs due to charge transfer between the metal and semiconductor, and the result is a space charge region in the semiconductor close to the M-S interface. This will cause a barrier to electron transport across the interface referred to as the Schottky barrier. The height of this barrier depends on the difference between the metal work function ϕ_m and the semiconductor work function ϕ_s. χ_s is the electron affinity of the semiconductor.

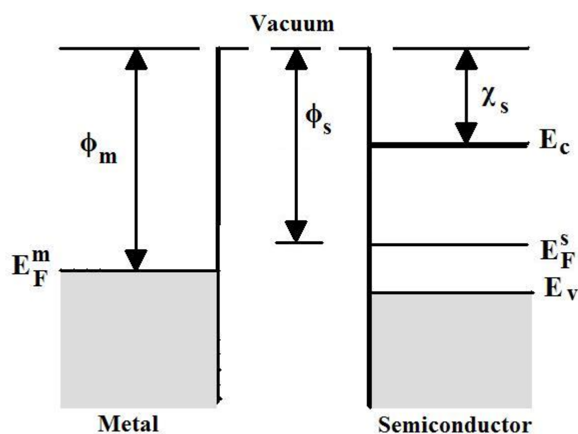

Figure 2.12: Energy band diagram for metal and p-type semiconductor in galvanic isolation. The essential parameters are included. Illustration based on illustration from [17].

Figure 2.13 shows the formation of a Schottky barrier for a p-type semiconductor. The position of the Fermi level in the band gap lies close to the valence band of the semiconductor, and after Fermi level alignment, the Schottky barrier is for injection of holes from the metal to the semiconductor.

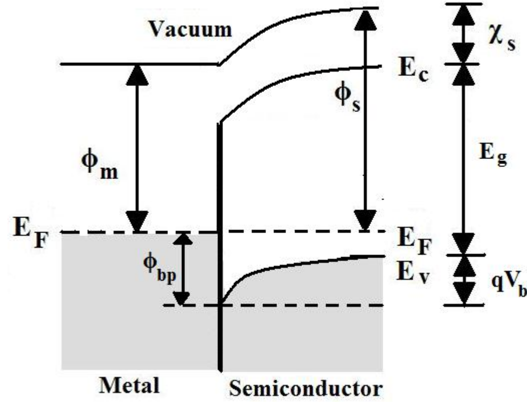

Figure 2.13: Schottky barrier for a metal/p-type semiconductor contact. Illustration based on illustration from [17].

ϕ_{bp} refers to the height of the Schottky barrier in this situation, and it is defined as

$$\phi_{bp} = \chi_s + E_g - \phi_m \tag{2.24}$$

Figure 2.14 shows the formation of a Schottky barrier for a n-type semiconductor. The Schottky barrier in this situation is given by

$$\phi_{bn} = \phi_m - \chi_s \tag{2.25}$$

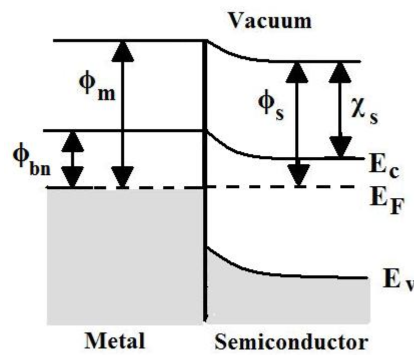

Figure 2.14: Schottky barrier for a metal/n-type semiconductor contact. Illustration based on illustration from [17].

For an n-type semiconductor, the Schottky barrier can be removed by choosing a metal work function ϕ_m which is lower than electron affinity χ_s of the semiconductor. This will cause a downward band bending in the semiconductor with electron accumulation near the semiconductor surface. This is the optimum situation for fabrication of ohmic contacts to n-type semiconductors [17]. When the semiconductor is p-type, a high work function metal is preferred [17]. This will reduce the height of the Schottky barrier, as can be seen from equation (2.24). For GaN, it is however difficult to remove the barrier completely because of the large energy band gap (E_g=3.4eV) and electron affinity (χ_s=4.1eV) of this material. This means that even when using metals with high work functions such as Pt (ϕ_m=5.6 eV) or Au(ϕ_m= 5.1 eV) a Schottky barrier $\geq$2 eV will exist.

It is reported that surface states in the semiconductor affect the band bending and barrier formation at the M-S surface in such way that the Schottky barrier is not only dependent on the metal work function [18]. The surface states are often related to various defects at the semiconductor surface [17]. Filling or emptying of surface states will together with space charge formation affect the barrier for electron/hole transport when a metal is placed in contact with the semiconductor. For a high density of surface states, the barrier will be nearly independent of the metal work function [17] and the Fermi level at the semiconductor surface is pinned to the energy position of the surface states [17]. This is why surface treatments such as cleaning and etching may affect the properties of M-S contacts [17].

2.3.4 Properties of Schottky diodes

Metal-semiconductor contacts with a Schottky barrier between the M-S surface are known as Schottky diodes [4]. Because there is a difference in the availability of charge carriers in the metal and semiconductor, the potential drops on the semiconductor side of the junction. This gives rise to a depletion region at the interface and is similar to what is observed in the p-n junction. In this case, the metal acts as a very heavily doped semiconductor material when considering the electrostatic properties of the depletion layer [4]. Schottky diodes have both rectifying and photovoltaic properties. The majority carrier flow is dependent on the Schottky barrier at the interface which varies with applied voltage [4]. This gives rise to a thermionic emission component of the current given by [4]

$$J_{0e} = A^* T^2 e^{-q\phi_B/kT}(e^{qV/kT} - 1) \tag{2.26}$$

where A^* is the effective Richardson constant and ϕ_B is the barrier at

the interface. This extra component of current is undesirable in photovoltaic energy conversion as it acts to increase the dark current of the diode and decrease the open circuit voltage. This means that the larger barrier ϕ_B, the better the performance. In figure 2.15 the illuminated characteristics of a Schottky diode are compared to a p-n junction device. Schottky diodes are simply made because no p-n junction formation is needed, but the performance is limited by the additional current given in equation (2.26).

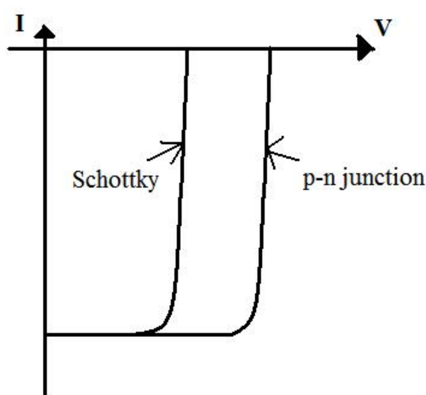

Figure 2.15: Illuminated characteristics of Schottky and p-n device. Illustration based on illustration from [4].

As mentioned in section 2.3.3, the size of the Schottky barrier is not only dependent on the metal work function, but also by Fermi level pinning close to the surface of the semiconductor due to induced surface states. This means that making a large Schottky barrier to improve the performance is not only dependent on the chosen metal work function but also the surface properties of the semiconductor material [17].

2.4 Hall effect and carrier concentration

The carrier concentration for a semiconductor can be calculated using the Hall effect. For the samples investigated in this thesis, the carrier concentration and the type of majority charge carriers are of importance to evaluate the semiconductor properties and to construct the p-IB-n device and Schottky diodes. The Hall effect relies on the displacement of moving charges in a magnetic field to determine the nature of the mobile carriers. The sample is placed such that the current flow is perpendicular to a strong magnetic field. The moving charges will experience a Lorentz force due to magnetic

induction $\boldsymbol{B}$ in the solid. This will generate a second electric field within the conductor, the Hall field, which is normal to both primary fields. If the current I is along the x axis and the magnetic field B is along the z axis, the charge carriers will be deflected in the y axis direction. This deflection will continue until the electric density is strong enough to oppose further charge displacements. The result is a Hall voltage along the y axis. The sign of the voltage will give the sign of the majority charge carriers [19].

The relationship between the current, magnetic induction and electric field is

$$\boldsymbol{E_y} = \pm R_H \boldsymbol{J_x} \boldsymbol{B_z} \tag{2.27}$$

where $\boldsymbol{E_y}$ is the electric field along the y axis, $\boldsymbol{J_x}$ is the current density along the x axis and $\boldsymbol{B_z}$ is the magnetic induction along the z axis. The constant of proportionality R_H, is the Hall coefficient. A positive Hall voltage compared with the orthogonal V, B and I axes gives a positive value of R_H and the material is p-type.

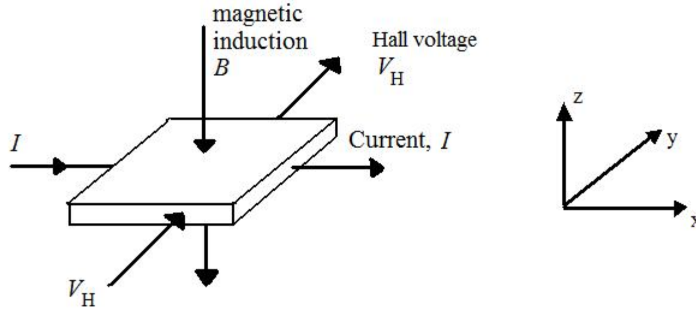

Figure 2.16: Arrangement of the measurements of the Hall effect, showing the axes used. Illustration based on illustration from [19].

The Hall coefficient is related to the number of mobile charge carriers. If the current is made up of electrons flowing parallel to x with a drift velocity v_x, the magnetic field present will make a force $\boldsymbol{F}$ on the electron given by

$$\boldsymbol{F} = e v_x \boldsymbol{B_z} \tag{2.28}$$

The force resulting from an electric field $\boldsymbol{E_y}$ on an electron is given by

$$\boldsymbol{F} = \boldsymbol{E_y} e \tag{2.29}$$

When the two forces are equal and equilibrium is obtained, $\boldsymbol{E_y} = v_x \boldsymbol{B_z}$. The current density is given by

$$\boldsymbol{J} = -n e v_x \tag{2.30}$$

where n is the number of mobile electrons per unit volume. This gives us the value of the constant of proportionality R_H as

$$R_H = -\frac{1}{ne} \tag{2.31}$$

The mobility derived from Hall measurements is often called Hall mobility to distinguish it from the drift mobility [19].

Chapter 3

Experimental techniques

In this chapter, the principles behind the experimental techniques used in this thesis are presented. Section 3.1 describes the principles behind the growth technique used to fabricate the ZnO:Co thin films. This is followed by different characterization techniques used to investigate structural, optical end electrical properties of the GaN:Mg and ZnO:Co samples.

3.1 Pulsed Laser Deposition (PLD)

Pulsed Laser Deposition is is a growth technique in which photon energy is coupled to the bulk starting material via electronic processes [20]. An intense laser pulse passes through an optical window of a vacuum chamber and is focused onto a solid or liquid surface, where it is partially absorbed. At a certain power density, the target produces an ejected luminous plume. The specific power density needed to produce this plume depends on the target material and the laser pulse wavelength and duration, but might be of the order of 10-500 MW cm^{-2} for ablation using ultraviolet (UV) excimer laser pulses of 10 ns duration [20]. Material from the plume recondenses on a substrate, where film growth occurs. The growth process may also include a passive or reactive gas or ion source.

The PLD technique has many advantages as a thin film growth technique. First, the laser is outside the vacuum chamber which provides a much greater degree of flexibility in material use and geometrical arrangements compared to vacuum-installed devices. In addition, almost any condensed matter material can be ablated. The pulsed nature of PLD means that film growth rates may be controlled to any desired amount and also the amount of evaporated source material is localized only to the area of the laser focus. The elemental components of the bulk and film are the same under perfect conditions, so

that even chemically complex systems can be deposited. Finally, the kinetic energies of the ablated species lie mainly in a range that promotes surface mobility while avoiding bulk displacements [20].

The disadvantages of the PLD technique is mainly that the targets may be impure and that macroscopic particles may be produced during the ablation process. Also, crystallographic defects may occur in the thin film because of bombardment by high kinetic energy ablation particles, but this is usually avoided as described above. There are also some variations in the flux and angular energy distributions within the ablation plume [20].

The physical processes in PLD are complex and depend on the laser pulse parameters and the properties of the target material. The most important are the light-material interaction and film growth [20].

3.1.1 Light-material interaction

The light-material interaction process strongly depends on the thermal diffusion length and the electric field involved in the PLD process. In this thesis, an excimer laser at 248 nm is used, so UV interactions is the most important process. When laser radiation is absorbed in the surface region of the target, the electromagnetic energy is converted into electronic excitation in the form of plasmons, unbound electrons and excitons in the case of insulators. The response within the material is dependent on the dielectric function $\varepsilon(\omega, K)$ and depending on the electronic band structure [20]. The electric field amplitude of the electromagnetic wave is given by [20]

$$E = \left(\frac{2\Phi}{cn\varepsilon_0} \right)^{1/2} \tag{3.1}$$

where Φ is the power density, ε_0 is the permittivity of free space, c is the velocity of light and n is the refractive index of the material. The threshold electric field strength for dielectric breakdown is hence proportional to the square root of the power density which is proportional to the laser fluence and inversely proportional to the laser pulse duration τ.

The material removal of the target can also be described by the rate of thermal conduction through the lattice. Using Fick's law of diffusion [20], the threshold fluence is proportional to $\sqrt{\tau}$. The excited electrons transfer their energy to the lattice within a few picoseconds and heating begins within the optical absorption depth of the material given by $1/\alpha$, where α is the optical absorption coefficient [20]. The thermal diffusion length is given by $l_t = 2\sqrt{D\tau}$, where D is the thermal diffusion constant. If this is smaller than the optical absorption depth, the target will be heated down to $1/\alpha$

independent of the pulse duration. In systems with multielemental targets, simultaneous evaporation is met if this condition is true. This is why fast UV lasers with small τ is preferred.

3.1.2 Film growth

PLD is often a preferred deposition technique because of its pulsed nature, the possibility of carrying out surface chemistry far from thermal equilibrium and the ability to reproduce the same elemental ratios in the thin films as in the target material [20].

Carrying out PLD in an ambient background gas, the film growth and chemistry may be enhanced or modified. The gases can be used to thermalize the plasma species through multiple collisions or to compensate for loss of an elemental component in the target material [20]. Compound targets are often used in PLD to make dielectric and ceramic films and other mulitelemental oxides or nitrides. This is one of the greate advantages with PLD compared to other deposition techniques [20]. Preparation of the targets may however propose some challenges. The sintering of the targets is an expensive and complicated process, and sample purity is rarely better than i part per 10 000 [20].

3.2 Scanning Electron Microscopy (SEM)

Scanning Electron Microscope is a type of electron microscope where high energy electrons are used to produce an image of the surface you are looking at [21]. In this thesis, SEM imaging is used to study the surface roughness of the GaN:Mg films and to measure the film thickness of the ZnO:Co films using cross section imaging. The principle is that the high energy electrons interact with the samples surface to produce a signal which later can be detected close to the surface.

The primary electrons hitting the samples produce signals coming from back scattered electrons (BSE) and secondary electrons (SE). Secondary electrons are produced when the high energy electrons from the source kicks out electrons from the surface. The signal detected from SE produces an image of the surface structure of the sample. It is possible to obtain ultra high resolution in this mode.

Back scattered electrons result from the primary electrons interacting with the sample surface and scattered within the material. The escape depths for BSE and SE are dependent on acceleration voltage and material, and BSE has longer depths than SE. Figure 3.1 shows the physical processes involved.

BSE may be used to produce elemental contrast as heavier elements reflect the electrons more. The resolution is lower in this mode since electrons below the surface may also escape.

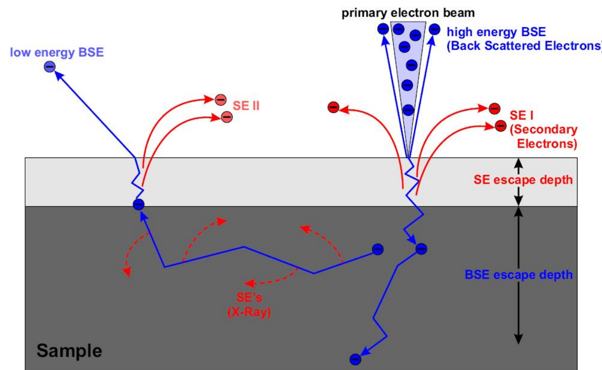

Figure 3.1: Physical processes involved in SEM imaging. Illustration from [21].

Acceleration voltage

The resolution in SEM imaging is strongly dependent on the acceleration voltages. The reason for this is that a higher acceleration voltage gives a bigger interaction volume which results in more scattering of the BSE electrons and SE produced further away from the primary electron beam. This reduces the resolution of the image. In light elements, the interaction volume increase more with acceleration voltage than for heavy elements, and in this way light elements are more sensitive [21].

3.3 Energy Dispersive X-ray (EDX) Microanalysis

In EDX analyzes, the X-rays are generated by an electron beam. A special sensor, usually a lithium-drifted silicon detector [22] is used to detect the X-rays which are characteristic for the different materials [21]. Figure 3.2a shown the concept of generation of x-rays from an electron beam. Secondary electrons escaping the atoms leave an unoccupied energy state in one of the lower orbital. An electron from a higher orbital relaxes down to the unoccupied energy state emitting a characteristic x-ray. The most common and easy observable transition are shown in figure 3.2b.

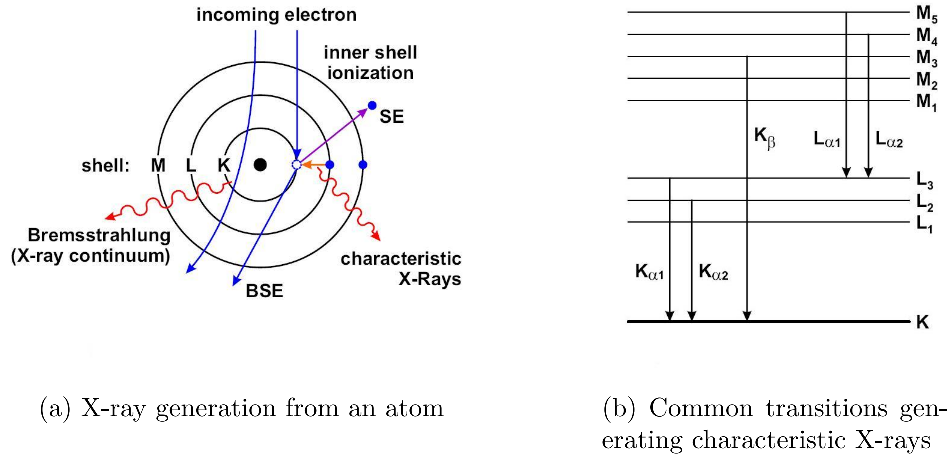

(a) X-ray generation from an atom

(b) Common transitions generating characteristic X-rays

Figure 3.2: Principles of EDX. Illustration is taken from [21].

In this thesis, EDX is used to identify and determine the ratio of the elemental components in the different samples. The ratio of the different elements is derived from the difference in intensity of the characteristic x-rays [22].

3.4 X-ray Photoelectron Spectroscopy (XPS)

X-ray Photoelectron Spectroscopy was used to study the valance state of the cobalt present in the low concentration ZnO:Co samples and to evaulate how much cobalt were present in each sample. X-ray Photoelectron Spectroscopy is an experimental technique that measures kinetic energy of electrons to determine electron binding energies in atoms and molecules. The basic principle is that photons with a specific energy excite the atoms which are below the surface of the sample. Electrons on the surface are released and detected close to the surface, and the energy spectra collected is used to find information about structure, concentration and chemical state [23]. XPS is a surface analysis technique with a depth of analysis of about 5 nm [24].

The kinetic energy of the released electrons are given by Einstein's law [25]

$$E_k = h\nu - E_b \tag{3.2}$$

where $h\nu$ is the energy of the incident radiation and E_b is the binding energy of the electron in a particular level of the atom. Because the incident photon energy is sufficiently large, many different levels in the sample may

be ionized and a spectrum is produced displaying all accessible energy levels as a distribution of photoelectrons with kinetic energies as given in equation (3.2). The intensity of the photoelectron peaks are labeled according to the quantum numbers of the level from which the electron originates. An electron has a total momentum number of $j = l + s$, where l is the orbital momentum number and s the spin momentum number, equal to 1/2 or -1/2. This is why, whenever $l > 0$, the peak is split into a doublet, with an energy difference called spin-orbit splitting [25].

The qualitative information, i.e. the valance state of the atoms are obtained from the energy position of a photoelectron peak with respect to the energy position of the same level in a reference compound [25]. This is called a chemical shift and is due to both different oxidation states and different chemical environments.

XPS may also be used as a quantitative technique. In this sense the number of electrons from a given transition that is recorded will be proportional to the element concentration. The accuracy for using XPS for quantitative analysis is about 10 % [23].

3.5 Optical transmission spectroscopy

Optical transmission spectroscopy was used to study the transmission and absorption in the ZnO:Co films. Transmission spectra provide information about the energy levels of the material and defects in condensed matter [26]. A light beam incident on the material surface will be reflected, absorbed and transmitted through the material depending on the optical properties of the material. The coefficient of reflectivity R is defined as the ratio of the reflected to the incident power and the transmittance T as the ratio of the transmitted to the incident power. If there is no scattering or absorption in the material, $R + T = 1$. Using a light source which radiates over a range of wavelengths, a transmittance spectrum $T(\lambda)$ can be obtained for the sample. Here, specific absorption levels in the material can be identified as characteristic absorption wells in the transmittance spectrum $T(\lambda)$.

3.6 X-ray Diffraction (XRD)

X-ray diffraction (XRD) is used for determining the arrangement of atoms in a material [27]. The principle is based on the diffraction that occur because the wavelength of x-rays is comparable to atomic spacing in the material. In this thesis, XRD is used to determine the orientation of the as-grown

ZnO:Co thin films grown on c-oriented sapphire substrate. The applications of XRD are many, including identification of components in a thin film, determination of which silicide is formed when a metal reacts with a substrate during heat treatment, determination of single crystal, polycrystalline or amorphous structures and preferred orientation in polycrystalline films [27].

The recorded XRD patterns consists of a series of intensity peaks as a function angle. Each peak in the spectrum corresponds to a specific atomic spacing d. The diffraction peaks are a result of Bragg's law of diffraction, which says that the relationship between the angle measured for each peak and the corresponding spacing d is given as [27]

$$n\lambda = 2d \sin\theta \tag{3.3}$$

where n is an integer, λ is the wavelength and θ is the angle the primary beam and the diffracted beam make with the plane. The diffraction pattern is characteristics for a material [27].

Chapter 4

Background research

The choice of studying cobalt doped ZnO for intermediate band (IB) material was partly done because of previous studies [28] which suggests it has a large potential for use in intermediate band solar cells (IBSC). Doping wide-band gap oxide semiconductors with transition metal impurities has been widely investigated as a strategy for extending the photoresponse of the semiconductor into the visible spectral range, making them suitable candidates for photochemical conversion of solar energy into electrical or chemical potential [28]. As described in the theory (section 2.3.1), deep level impurities in bulk materials may form an IB within the band gap when introduced at sufficient high concentration. In this chapter, previous research on the properties of ZnO:Co are being presented in relation to the possibility for using this material in IBSC. The chapter also includes previous research on GaN:Mg and ZnO:Al which was aimed to be used as the p- and n- emitter respectively in the implementation of the IBSC in this thesis. Finally, previous research on ohmic and Schottky contacts to GaN and ZnO are discussed, which will be used for making an IB-device in this thesis.

4.1 ZnO:Co

ZnO is a semiconductor material with a large direct bandgap of 3.3 eV and a large exciton binding energy of 60 MeV [29], higher than for some widely used wide-band-gap materials, such as ZnSe (20 meV) and GaN (21 meV) [30]. It is an abundant resource and has high thermal and chemical stability. The material has been used for applications such as catalysts, ceramics and rubber additives [31]. Today, much of the research on this material is related to its potential for use in optoelectronic devices such as solar cells, electrodes, sensors, transparent UV-protection films and UV light emitting devices [31].

ZnO has wurtzite crystal structure at ambient conditions [32] and a strong ionic bonding where the conduction band mainly comes from Zn^{2+} $4s$ states and the upper valance band arises from O^{2-} $2p$ states together with Zn^{2+} $3d$ states [33]. Undoped ZnO exhibits n-type conductivity due to donor-type defects such as oxygen vacancies (V_O) and zink interstitials (Zn_i) [34]. In figure 4.1, the hexagonal wurtzite structure of ZnO is illustrated.

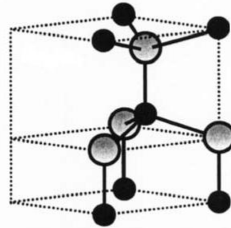

Figure 4.1: Hexagonal wurtzite structure of ZnO. The shaded gray and black spheres represents Zn and O atoms respectively. Illustration taken from [32].

Cobalt is a transition metal element and can excist in many electron states. It is reported [31] that doping ZnO with appropriate amount of Co, both the optical and magnetic properties of ZnO can be tuned without changing the crystal structure. Much of the research concerning cobalt doped ZnO focuses on the behavior as diluted magnetic semiconductor and its magnetic properties [29][35][36][37][38][39]. The observation of room temperature ferromagnetism [35] in cobalt-doped ZnO has made it a promising candidate material in the field of spin-electronics. Since this thesis focuses on the use of ZnO:Co as a possible IB material, the structural, optical and electrical properties from previous research is presented while the magnetic properties are not discussed further.

4.1.1 Pulsed Laser Deposition of ZnO, ZnO:Co and ZnO:Al

The literature reports on several experiments where thin films of ZnO, ZnO:Co and ZnO:Al have been made by PLD. Because deposition parameters such as substrate temperature, target-substrate distance, laser pulse energy and ambient oxygen pressure affect the physical properties of ZnO layers grown by PLD, it's important to have an understanding of previous experiments carried out. For the growth of ZnO by PLD technique, usually UV excimer lasers such as KrF (λ= 248 nm) and ArF (λ= 193 nm) or Nd: yttrium aluminum garnet (YAG) pulsed lasers (λ= 355 nm) are used for ablation of the ZnO target in an oxygen environment [32].

In [40], two series of ZnO thin layers were grown on Si (1 1 1) substrates by PLD. The ZnO layers were prepared either from a pure metallic Zn target disc or from a hot-pressed ceramic ZnO target disc to study the effects of oxygen atmosphere on the structural properties of ZnO layers [40]. High-purity oxygen at pressure levels of 1, 5, 10, 15, 25, and 35 Pa was maintained in the chamber. The ZnO layers were prepared with a substrate temperature of 400 ° C with 2.8 J/cm2 laser energy fluence, 120 mJ energy per pulse, 10 Hz pulse repetition rate, and 15 000 laser pulses (approximately 25 minutes). Depending on the ambient oxygen pressure levels the thicknesses of layers varied from 200 to 1200 nm from higher to lower pressure. The ZnO layers grown from the Zn target were thinner than those grown from the ZnO target [40].

PLD growth of cobalt-doped ZnO with ZnO:Co targets are reported in several publications [35] [41] [36]. In [35], targets containing 0, 2, 5, 10, 15 and 30 % cobalt were ablated using a KrF eximer laser with a repetition rate of 1 Hz and a laser energy density of 1-3 J/cm^2. The target-to-substrate distance was 5.5 cm, the temparature was in the range from 400-600 ° C and oxygen pressures up to 0.02 mTorr were used. The films were deposited on *c*-plane oriented sapphire substrates. Another study [41] reports on the deposition of ZnO:Co films containing 25 % cobalt on the same substrate using sintered targets of ZnO:Co. In this research, the KrF laser used had a repetition rate of 5 Hz and a laser energy density of 1.5 J/cm^2. The target-to-substrate distance was 4 cm, and the temparature was varied from 400-700 ° C. The oxygen pressure was kept constant at 0.1 mTorr. In [36] targets with cobalt concentration from 1-15 % were ablated onto R-cut sapphire substrate. The KrF laser used had a repetition rate of 10 Hz and a laser energy density of 1.8 J/cm^2. The temperatur and pressure were kept constant at 600 ° C and the target-to-substrate distance was 3.5 cm.

The crystal structure of the thin films grown by PLD was determined by X-ray diffraction (XRD). The films grown on *c*-plane sapphire substrates [35] [41] showed intense peaks corresponding to hexagonal wurtzite ZnO structure. In [41], where the temperature was varied from 400-700 ° C, the $\theta - 2\theta$ angular scans showed homogeneous alloy ZnCoO films for low temperatures ($\leq 600°$), while at higher temperatures wurtzite ZnCoO, rock-salt CoO and hexagonal Co were detected. This means that the solubility of Co ions in ZnO depends on the growth condition [41]. In [35] they observed a small peak around 2θ=44.4° for the high concentration samples which indicates cobalt containing phases of cobalt oxides or cobalt metal. At higher growth temperatures, the cobalt precipitated out of the lattice as CoO. This is consistent with what they observed in [41]. In [35] they also observed that the Co metallic phase disappeared from the XRD scans when increasing the base

pressure to >0.1 mTorr or adding a small amount of oxygen. The films grown on R-cut sapphire substrates also shows hexagonal wurtzite structure with (1 1 0) texture [36]. No other impurity phases were detected from the XRD scans in this research.

X-ray Photoelectron Spectroscopy was also used in [35] to evaluate the valance state of the Co in the ZnO films prepared by PLD. If Co is substituting Zn in the ZnO lattice, a valance state of Co^{2+} should be detected [29]. The XPS spectrum of the Co 2p binding energies was recorded for the ZnO:Co films after sputtering the film for 5 min with Ar^{+} ions to reduce surface contamination. They observed a $2p_{3/2}$ peak located at 780.5 eV which is due to the Co^{2+} oxidation state. They found that the energy separation between the $2p_{3/2}$ and $2p_{1/2}$ was Δ = 15.6 eV which are consistent with divalent cobalt. A lower binding energy $2p_{3/2}$ peak at 778 eV with Δ=15 eV was observed for the 30 % cobalt concentration films after Ar^{+} sputtering, which is attributed to cobalt metal. Metallic cobalt clustering beneath the surface of the film may be the reason for this peak [35].

The PLD growth of Al-doped ZnO film on sapphire using a GaN buffer layer is reported in [42]. The GaN layer is used because sapphire and ZnO have a large lattice mismatch (16.8 %), which will indruduce a high density of dislocations [42]. GaN and ZnO have a lattice mismatch of only 2.2 %, so GaN is a more suitable substrate for growing epitaxial films of ZnO. The GaN buffer layer were grown by PLD, and the thickness of the GaN film were found to be 1.8 μm. For growing the ZnO:Al layer, a 2 in. in diameter ZnO target doped with 2 wt % Al_2O_3 was used. The ZnO:Al films were deposited at different oxygen pressures varying from 0.1 to 10 mTorr and different pulse repetition rates from 5 to 10 Hz. The substrate tamperature was varied from 300 to 400 ° C and the deposition time was kept at 60 minutes [42]. After deposition, the films ZnO:Al film thickness' were measured to be in the range from 0.5 to 0.9 μm. The chararterization of the films showed that the films grown at low substrate temperatures had poor quality. The reason for this could be that at low temperatures, a surplus of Zn will form Zn clusters. At higher temperature, such a process is reduced because of compting process of surface migration and re-evaporization [42].

4.1.2 Optical properties of ZnO:Co

The optical properties of ZnO has been widely studied by other research groups because of its potential for blue and ultraviolet optical devices such as light emitting diodes (LEDs) and laser diodes [42]. In [29], optical properties of Co-doped films are being studied using UV-vis transmittance spectra. The ZnO film showed an average transmittance above 85 % and an absorption

edge at 380 nm. When increasing the cobalt concentration, the transparancy of the films was weakened. This is due to the increased darkening of the green color in the films, assigned as d-d transitions of high spin states Co^{2+} $3d^7(^4F)$ in a tetrahedral oxygen coordination [29]. In addition, strong absorption were found around 660, 615 and 560 nm in the visible range. The three absorption lines are assigned to the crystal field transitions $^4A_2(F) \rightarrow ^2 E(G)$, $^4A_2(F) \rightarrow ^4 T_1(P)$ and $^4A_2(F) \rightarrow ^2 A_1(G)$ respectively [29]. These are d-d transitions between donor and acceptor ionization levels located within the band gap of the host ZnO, which are possible in Co^{2+} with $3d^7$ high-spin configuration under a tetrahedral crystal field [43]. They also abserved a red shift in the absorption edge with increasing Co content. E_g of the Co-doped ZnO films were determined by ploting the absorption coefficient α^2 as a function of photon energy $h\nu$. The value of α for different wavelength was determined by using the relation [29]

$$\alpha = -\frac{1}{D} \ln T \tag{4.1}$$

where D is the film thickness and T is the transmittance. The result showed a decrease in E_g from 3.27 to 2.88 eV with increasing Co content from 0 to 15 %. The red shift is explained by sp-d exchange interactions between the band electrons in ZnO and localized d electrons in Co^{2+} [29].

The optical properties of ZnO:Co was also investigated in [31]. The prepared samples were studied by UV-vis absorption and photoluminescence (PL) spectra. They observed the same three absorption lines in the visible spectral range of the cobalt doped films. A large red-shift of the absorption edge was also observed with increasing cobalt content. The wavelength of the absorption edge was determined by extrapolating the linear part of the absorbance to A(λ) = 0. The band gap energy decreased from 3.11 to 2.62 eV with increasing cobalt concentration from 0 - 10 %. PL was used to further measuring the band structure of the semiconductor material. All the samples investigated (up to 10 % cobalt concentration) showed a emission peak in the UV region, assigned as a near-band-edge (NBE) emission from the direct exciton recombination. No other visible emissions were detected in the spectra.

4.1.3 Electrical properties of ZnO:Co

Both undoped and cobalt doped ZnO shows n-type conductivity where the carriers are probably associated with oxygen vacancies [36]. The intrinsic carrier concentration of ZnO is $\leq 10^6$ cm^{-3}, while the maximum n-type doping is found to be $\geq 10^{20}$ cm^{-3} electrons [44]. In [36] they report that resistivity

in the ZnO thin films increased with increasing cobalt doping concentration, and for the 7% cobalt sample the room temperature resistivity was ≥ 200 Ω-cm. In [28], where nanocrystalline Co^2:ZnO films with 3% cobalt were studied, the resistances were beyond the upper limit of the detection capabilities ($\geq 10^9\Omega$). The carrier concentration of Co-doped thin films was determined in [29], and all the samples containing 5, 10 and 15 % cobalt respectively had a carrier concentration above 10^{19}cm^{-3}.

4.2 GaN:Mg

GaN is chosen as the p-type material for the p-IB-junction investigated in this thesis because of its properties as transparent direct wide-band gap (3.4 eV) semiconductor and possibility for p-type conductivity when doped with Mg-atoms [45]. It has wurtzite structure which is the same crystal structure as ZnO and the lattice mismatch between ZnO and GaN is within 4%. GaN-devices are videly used in optoelectronic devices such as LEDs and laser diodes for applications such as displays, lighting and data storage. The devices require good contacts to p-doped GaN. Despite the high concentration of Mg dopants, GaN suffers from low conductivity. For fabrication of GaN photonic devices, sapphire ($\alpha - Al_2O_3$) is the preffered substrate because of chemical stability, wide ability and comparatively low price of large sapphire wafer [17].

4.2.1 Pre-treatments of Mg-doped GaN

When growing GaN, a number of vacancies is created which contribute to n-type doping. Also, shallow acceptor dopant has not been found for GaN [17]. The samples investigated in this study are doped with Mg, which is the most common p-type doping material. However, it is a deep acceptor with its activation energy of 0.14 - 0.21 eV [17]. Hydrogen contamination from growing the GaN will form Mg-H-complexes witch are electrically inactive [17] and will reduce the doping efficiency even more. To increase the conductivity of the material, several methods of pretreatments have been suggested by different research groups. In [46], the pre-treatment consists of an RTA process at 950°C for 60 s in N_2 ambient. This activation resulted in a hole-concentration of 2-4x10^{17} cm $^{-3}$ and a hole-mobility around 10 cm^2/Vs.

Another research group [47] tried several different pre-treatments to compare the different techniques. They use both one- and two- step rapid thermal annealing (RTA) for activating Mg-doped p-type GaN films and compared with conventional furnace annealing (CFA). RTA has been a preferred tech-

nique in activating dopants in semiconductors and avoids dopant redistribution due to shorter annealing time as compared to CFA. The ramp-up temperature was 100°C/s. The one-step RTA annealing was conducted in 600°C for 15 min, the two-step RTA annealing was conducted at 750°C for 1 min (first step) and 600°C for 5 min (second step), and the CFA process was conducted at a constant temperature of 700°C for 30 min. All the processes were carried out in both oxygen and air ambient. The initial Mg doping concentration of the samples were in the range of 2-3 x $10^{19} cm^{-3}$. When comparing the samples annealed in oxygen ambient to those in air ambient, the electrical properties of the samples were better in the samples annealed in oxygen. Also, the two-step annealing shows higher hole concentration and lower resistivity in the treated samples than the CFA and one-step RTA. The two step annealing in oxygen ambient shows a better result in activating p-type GaN films with highest hole concentration of 6 x $10^{17} cm^{-3}$, compared to 2.1 x $10^{17} cm^{-3}$ of the CFA annealing in the same ambient. The one step RTA shows a hole concentration of 2.0 x $10^{17} cm^{-3}$. The resistivities for the three different recipes is 4.5 Ω cm, 7.5 Ω cm and 6.0 Ω cm for the two-step RTA, one step RTA and CFA respectively. The research suggests that the high temperature process could effectively break the Mg-H bonds and the low temperature process could further activate Mg acceptors in two step annealing.

In [48], the Mg acceptors of GaN films are activated as p-type GaN with rapid thermal annealing and furnace treatments. The as-grown GaN:Mg films were activated in N_2 ambient for 30 min with varying temperatures of 600, 700, 800 and 850°C in the furnace system. The other series of Mg-doped GaN was activated by the RTA system and the temperature was varied from 600 to 960°C for 1 min. Using the van der Pauw method in the Hall effect measurement, ohmic properties were observed for all of the activated GaN:Mg films from the current versus voltage (I-V) curves. They found that the optimum activation temperatures are located at 700 and 800°C in the furnace and RTA systems respectively. For good device performance, the p-type GaN must have a high hole concentration, a high mobility and a lower bulk resistance [48]. Comparing the optimum electric properties of GaN:Mg films in the RTA at 800°C and furnace at 700°C activation systems, the active hole concentrations were similar and the hole mobility was higher for the GaN:Mg films with 800°C RTA treatment. The maximum hole concentration of 3.6 x 10^{17} cm^{-3} and hole mobility of 9.2 cm^2/V s were obtained with the furnace treatment at 700°C annealed for 30 min. The resistivity after this treatment was 1.6 Ω cm. For the RTA process at 800°C the hole concentration, mobility and bulk resistance were 2.4 x 10^{17} cm^{-3}, 12 cm^2 /V s and 1.6 Ω cm for this p-type GaN film. The surface states of the GaN:Mg films were damaged at

high temperature RTA treatments. The conclusion from this paper is that the RTA activation system provides a fast, low-temperature process with better electric properties for p-type GaN:Mg activation than the furnace treatment.

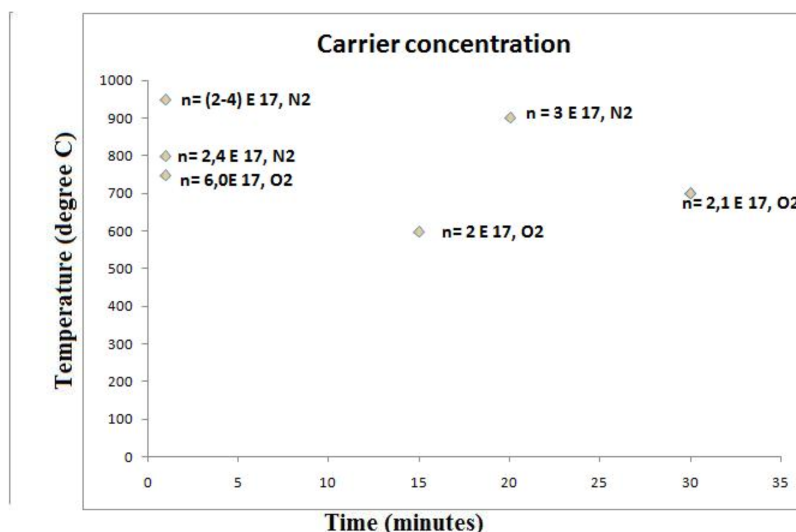

Figure 4.2: Carrier concentration at different temperature / time

In figure 4.2, the carrier concentrations obtained from the different RTA experiments described above are plotted. The highest carrier concentration is obtained for the two step RTA process in oxygen ambient. Table 4.1 shows the results from the different experiments with the essential parameters included.

Table 4.1: Overview of the different activation processes

Process	Temperature (° C)	Time (min)	Ambient	Initial Mg doping	Carrier concentration (cm^{-3})	Hole mobility (cm^2/V s)	Resistance (Ω)
RTA	950	1	N_2	-	2-4 x 10^{19}	10	-
RTA	600	15	O_2	2-3 x 10^{19}	2 x 10^{17}	-	7.5
Two-step RTA	750/600	1/5	O_2	2-3 x 10^{19}	6 x 10^{17}	-	4.5
CFA	700	30	O_2	2-3 x 10^{19}	2.1 x 10^{17}	-	6.0
CFA	700	30	N_2	-	3.6 x 10^{17}	9.2	1.6
RTA	800	1	N_2	-	2.4 x 10^{17}	12	1.6

4.3 Ohmic contacts for GaN- and ZnO-devices

Ohmic contacts to GaN and ZnO are needed to study the performance of the junction devices and to measure the carrier density in the samples. Because

of the large bandgap of GaN, it is a challenge to fabricate good ohmic contacts because of the tendency to form a large Schottky barrier. In semiconductor manufacturing, ohmic contacts are commonly made by heavy doping of the surface layer providing a thin Schottky barrier that permits current transport by quantum mechanical tunneling [17]. For p-type GaN, this is difficult because high effective p-type doping is difficult to achieve. The most common contacts to GaN are Au/Ni annealed in various ambients [17]. The reason for this is that both Au and Ni have high metal work functions. Au is very conductive and non-oxidating, while Ni is a reactive metal with good adhesion to GaN surface, so mixing these two materials before sintering will make good ohmic contacts [17].

Ohmic contacts to n-type ZnO are commonly made by depositing two layers of Ti and Au on the ZnO surface [49][50]. In [49], the contacts were made by electron-beam-deposition of 25 nm Ti followed by 100 nm Au. The contacts showed ohmic behavior with contact resistivity in the range of 3 x $10^{-4}\Omega\ \mathrm{cm}^{-2}$ regardless of the polarity (Zn face or O face)of the ZnO substrate. Annealing the contacts had little effect of the contact properties. In [50] they used the same deposition technique but the thickness of the Ti and Au layer was 30 and 50 nm respectively. These contacts were also ohmic, but the contact resistivity was in the order of 2 x $10^{-2}\Omega\ \mathrm{cm}^{-2}$. After annealing the samples, the contact resistivity was reduced to the order of 2 x $10^{-4}\Omega\ \mathrm{cm}^{-2}$. The reason for better contact quality before annealing from [49] could be due to different surface cleaning procedures before deposition. In [49] the samples were degrease in acetone and methanol prior to the metal deposition, while in [49] the surface was ultrasonically degreased in trichloroethylene, acetone, and methanol, and rinsed in deionized (DI) water for 5 min. Then the samples were etched using $HCl:H_2O$ (2:1) to remove native oxide, and blown dry with N_2. The literature also report on other metals used to form ohmic contacts to ZnO including Al/Au [51] and Pt/Ga [52].

4.4 Schottky contacts for ZnO-devices

Schottky contacts to n-ZnO are studied for the possibility of making Schottky diodes of the ZnO:Co thin films. The literature reports on several different metal contacts which gives a Schottky barrier between the M-S surface such as Au [53] [54], Pd [55] [56], silver oxide [56] and Pt [57] [56].

In [53] a conventional Schottky diode was made by depositing Au on the ZnO surface by electron beam evaporation. Room temperature I-V characteristics showed Schottky behavior with reverse-bias leakage current of -0.056 mA to 1V reverse bias and an ideality factor m of 1.9 with a Soft breakdown

at -2 V.

In [56], Ni, Ir, Pd, Pt, and silver oxide Schottky contacts on the Zn-polar face of hydrothermally grown bulk ZnO were examined to find a relationship between the Schottky barrier height (SBH) and the free energy of the metal oxide formation. Before metalization, the ZnO wafers were cleaned ultrasonically in acetone and then rinsed in methanol and isopropyl alcohol. After deposition of Schottky contacts, Ti/Al/Pt Ohmic contacts were fabricated around each Schottky contact and the diodes were characterized by current-voltage (I-V) and capacitance-voltage (C-V) measurements at room temperature. The ideality factor m for the different Schottky contacts were $m_{Ir} = 3.5$, $m_{Pd} = 2.0$, $m_{Pt} = 2.0$ and $m_{silveroxide} = 1.06$. The Ni contact showed ohmic behavior. The non-idealities of the Schottky diodes were explained by metal oxide formation at the interface. This will result in an increase in the density of oxygen vacancies (V_O)close to the interface [56]. The energy level of V_O is placed at approximately E_C -0.7 eV [56], so Fermi level pinning at the ZnO surface will occur, reducing the SBH.

Chapter 5

Equipment and Techniques

In this chapter, the experimental procedures are presented. The GaN:Mg wafer which was intended to be used as substrate for making GaN:ZnO diodes and GaN:Mg-ZnO:Co-ZnO:Al p-IB-n junctions are purchased from Technologies and Devices International, Inc. The thickness of the wafer is 7 μm and the sapphire is polished on both sides to facilitate optical characterization.

The ZnO samples containing 1, 2 and 5 % cobalt deposited by PLD on sapphire and silicon substrates were made by Cecile Ladam at SINTEF Trondheim during summer 2010. They are referred to as the low concentration samples in the rest of this thesis. The other samples containing 10, 20 and 30 % cobalt concentration deposited on sapphire substrates are referred to as the high concentration samples.

5.1 Cleaning procedure for GaN:Mg wafers

To make a clean GaN surface before activating it in a Rapid Thermal Process (RTP) Unit, a chemical cleaning process was used. The samples were first put in a solution of acetone and rinsed in ultrasonic bath at 60° C for 10 minutes. After this, the samples were transferred to a ethanol solution and rinsed in the ultrasonic bath for 10 more minutes. Finally, the samples were cleaned with deionized water before they were dried with a nitrogen gun.

5.2 Activation of GaN:Mg

To activate the Mg in p-doped GaN wafers, the Rapid Thermal Process (RTP) Unit at NTNU Nanolab was used. The instrument is a JetFirst 200 Processor which includes a stainless steel chamber for rapid thermal heating under controlled atmosphere or vacuum [58]. The temperature range is up

to 1200° C with a maximum heating range of 100° C/s. Both oxygen and nitrogen ambients may be used in this unit. Initially, several different recipes were carried out to determine which process gave the highest carrier concentration of the activated samples. The best recipe was then applied to the remaining samples. Table shows the different recipes used in the RTP.

Table 5.1: Different recipes used in the RTP

Temperature [° C]	Ramp up rate [° C /s]	Time [min]	Ambient
900	10	1	N_2
950	10	1	N_2
1000	10	1	N_2
580	10	15	O_2
620	10	15	O_2

5.3 Dry etch of GaN

Because initial Hall measurements on the GaN:Mg wafer showed n-type conductivity and the manufacturer of the wafer confirmed that SIMS profile performed showed presence of thin $\sim$ 100 nm layer on top that contained unintentional high background Si that may cause the Hall measurements being unable to confirm p-type conductivity, samples from the GaN wafer were etched in a Inductive Coupled Plasma Reactive Ion Etch (ICP-RIE) system. The system is a PlasmaLab system 100 ICP-RIE, Tool number 1230. Different recipes were tested and the etch rate for the different recipes were determined by measuring the film thickness with a reflectometer before and after etch. The reflectometer is a Filmetrics F20 thin-film analyzer. Before and after etching the samples were cleaned in successive ultrasonic baths of acetone and ethanol. The different recipes used in the ICP-RIE are shown in table 5.2.

5.4 Pulsed Laser Deposition (PLD) of ZnO:Co high concentration samples

Different samples have been grown at the Pulsed Laser Deposition (PLD) lab in the electro building at NTNU. The setup uses a Pfeiffer vacuum system. Table 5.3 gives an overview of the different samples grown and the most

Table 5.2: Different recipes used in the ICP-RIE

	Recipe 1	Recipe 2	Recipe 3
Ar [sccm]	20	20	20
Cl_2 [sccm]	20	20	20
Pressure [mTorr]	5	5	5
Temperature [° C]	20	20	20
ICP power [W]	2000	2000	2000
RF power [W]	20	10	20
DC [V]	60-120	84	60-120
Time [min:sec]	10:00	01:00	00:30

important parameters used during deposition. A full overview of all the parameters for the different samples is included in appendix A. The targets used to grow films of ZnO:Co have been fabricated by Tommy Mykkelbust at SINTEF Trondheim. They are composed of ZnO doped with cobalt with 10, 20 and 30 % doping level.

The targets were glued to a target holder and polished before inserted into the deposition chamber. The substrates were cleaned sequentially in acetone and ethanol by an ultrasonic cleaner, then dried with nitrogen gas. The substrates were mounted mechanically to a sample holder to avoid using silver glue on the back side of the substrates to facilitate optical characterization after growing the films.

Before deposition, the targets were pre-ablated for 10 minutes to clean the target surface. During deposition, the target scans at a diameter of 12 mm to obtain uniformly thick films.

The substrates were placed parallel to the target surface at a distance of 45 mm, the incident angle between the target surface and laser beam being 45 °. Before deposition the vacuum chamber was pumped down to 10^{-2} mbar. A pulsed KrF LPX *Pro* laser (λ= 248 nm) was used for targets ablation. ZnO layers were prepared at a temperature of 450 ° C with 10 Hz pulse repetition rate. A schematic diagram of the pulsed laser deposition experimental set-up is shown in figure 5.1.

5.5 Contact metalization of GaN:Mg and ZnO:Co

Preliminary contacts to make initial Hall measurements of the activated GaN:Mg films were made by liquid Indium-Gallium pasted on the corner

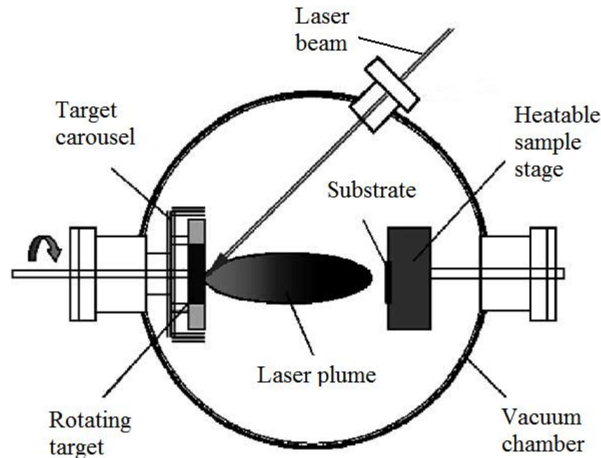

Figure 5.1: Schematic diagram of the pulsed laser deposition experimental set-up. The illustration is based on illustration from [59]

Table 5.3: Overview of samples deposited by PLD

Sample ID	Substrate	Target	Dep. duration[min]	[W] Power on the target	T setpoint [°C]	Laser pulse rep. rate [Hz]
ZC110201	p-Si(001)	ZnO:Co(10%)	67		450	10
ZC110301	c-sapphire	ZnO:Co(10%)	65		450	10
ZC110302	c-sapphire	ZnO:Co(20%)			450	10
ZC110401	c-sapphire	ZnO:Co(30%)			450	10

of the samples. The contacts were made as small as possible to minimize the error of the Hall measurements. The contact configuration is shown in figure 5.2b.

5.5.1 Electron Beam Evaporator

To make ohmic and Schottky metal contacts to the ZnO:Co semiconductor surface, the Electron Beam Evaporator at NTNU NanoLab was used. This is a Pfeiffer vacuum classic 500 system. For the ohmic contacts, two layers of 50 nm titanium and 200 nm gold were deposited on the corner of the sample surface with an aluminum foil as a mask. The contact configuration is shown in figure 5.2a. This procedure is similar to what they reported in [57] and [49], which gave good ohmic contacts.

To make Schottky contacts a 800 nm layer of gold was deposited in the

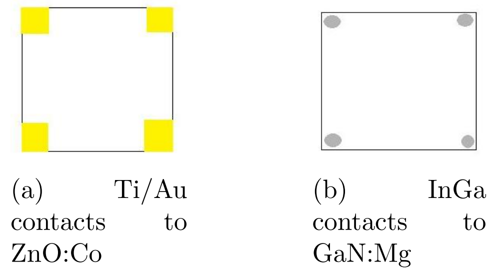

(a) Ti/Au contacts to ZnO:Co

(b) InGa contacts to GaN:Mg

Figure 5.2: Contact configuration

center of the samples using aluminum foil as a mask. Gold is reported to form a Schottky barrier to ZnO [53] [54]. Because these contacts did not show Schottky I-V characteristics, a second run of deposition of 80 nm platinum was done using aluminum foil as a mask. Platinum has a higher metal work function than gold (5.6 eV for Pt compared to 5.1 eV for Au) and should form a large Schottky barrier to n-type ZnO [17]. Before contact deposition, the sample was cleaned with ultrasonic baths of acetone and ethanol. The contact configuration for the Schottky contacts is shown in figure 5.3.

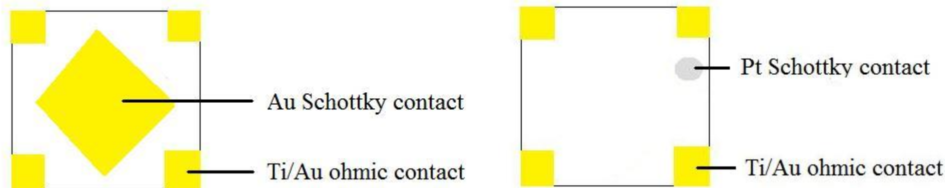

Figure 5.3: Contact configuration for the Schottky contacts

5.6 Hall measurements of GaN:Mg and ZnO:Co samples

The Hall measurements were carried out in Electro Building at NTNU. The instrument used was a Lakeshore Model 7504 Hall system controlled by a PC program. Both the sample resistivity, carrier concentration and dark I-V measurements were carried out using this setup. The sample is mounted to a probe station where four probes are connected to the four contact points on the sample surface. The sample holder is then placed in a magnetic field. A

current is driven between two of the contacts, while the voltage is measured from the two others. For resistivity estimates, the current is sourced between contacts 1 and 2 and the voltage is measured between contact 3 and 4. For measuring the hall voltage and hence the carrier density, the current is sourced between contacts 1 and 3, and the voltage is measured between contacts 2 and 4. For the dark I-V measurements, both the current and the voltage is measured between all contact pairs 12, 23, 34 and 41. The configuration of the sample holder with the four contact points is shown in figure 5.4.

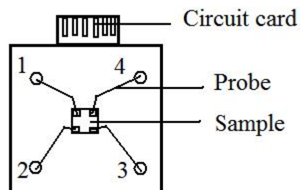

Figure 5.4: Sample holder in the Hall measurement setup.

5.6.1 Additional I-V measurements of ZnO:Co Schottky diodes

To measure the Schottky diode properties of the Au and Pt Shottky contacts to ZnO:Co, dark I-V curves was recorded using a setup at the Solar Cell Characterization Lab at Natural Science Building at NTNU. The setup includes a Keithley 2440 sourcemeter controlled by a PC program and a probe station for mounting the samples. This setup was preferred over the Hall measurement setup because the force applied from the probes can be adjusted to a minimum to avoid the probes penetrating the metal layer. The accuracy is limited by the amount of stored digits in the output data files, which is $\pm 1\mu V$ and $\pm 1\mu A$ for the voltage and current respectively [60].

5.7 Scanning Electron Microscopy (SEM) of GaN:Mg and ZnO:Co samples

To examine surface roughness of the activated and etched GaN:Mg samples and to measure film thickness of the ZnO:Co samples, Scanning Electron Microscopy was used. A S-5500 (In-lens) ultra high resolution S(T)EM was used to produce high resoloution surface pictures while a Hitachi TM3000

table top SEM was used as a quick method for identifying larger impurities on the surface. The table top SEM allows for large samples (70 mm diameter and 55 mm hight) while the S-5500 S(T)EM has sample restrictions of 9.5 mm x 5.5 mm x 1.0 mm.

5.8 Energy Dispersive X-ray (EDX) analysis of GaN:Mg and ZnO:Co samples

The EDX analysis were done at the table top SEM at NTNU NanoLab. The SEM includes a Quantax EDX-system from Bruker. The EDX system was used to determine the ration of Ga and N in the GaN:Mg films before and after etching in the ICP-RIE.

5.9 Optical Transmission Spectroscopy of ZnO:Co samples

To measure the optical transmission of the thin films, optical transmission spectroscopy was performed. The setup uses a ThorLabs Compact fiber spectrometer CCS100 together with a Mini-D2T lamp from Ocean Optics. Additional measurements were done using an AvaSpec spectrometer from Avantes. The experiments were done at Professor Ursula Gibsons lab in U4 in Natural Science Building at NTNU. The spectrometer measures wavelengths in the range from 300 - 750 nm. A sapphire sample was used as reference and all the samples deposited on sapphire substrate were measured.

For further analysis of the optical properties, the thickness of the samples was determined by SEM cross section imaging and by using a Veeco dektak 150 profilometer.

5.10 X-ray Photoelectron Spectroscopy (XPS) of ZnO:Co low concentration samples

The XPS experiment was carried out by Spyros Diplas at MiNaLab in Oslo in the fall 2010 for the low concentration samples. The instrument used was a Kratos Axis UltraDLD using an A1 K_α X-ray source. The samples were cleaned with isopropanol prior to the experiment to reduce surface contamination. To reduce charge accumulation on the surface of the samples, the samples were partly in contact with grounded copper metal. To determine

the chemical composition of the thin films, a survey spectrum of the different samples was recorded. High resolution spectra for the different elements O, Zn and Co were also recorded to get additional information, i.e. the valance state of Co in each sample. The data were analyzed using the software Casa XPS.

5.11 X-ray diffraction (XRD) of the ZnO:Co samples deposited on sapphire substrate

X-ray diffraction (XRD) was used to determine the crystal orientation of the ZnO:Co thin films grown on c-oriented sapphire substrate. The instrument used is a D8Discover diffractometer. A schematic of the setup is shown in figure 5.5.

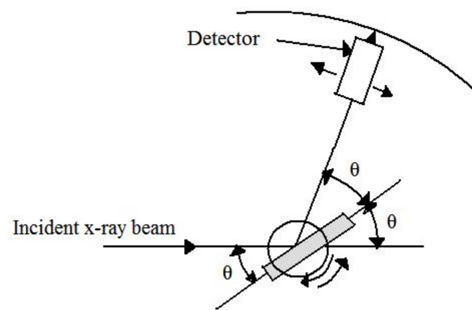

Figure 5.5: Diffractometer schematic. The illustration is based on illustration from [61].

During the scan, the crystal is rotated by θ while the detector are is rotated by 2θ recording a θ-2θ scan for the sample investigated. The intensity peaks recorded is used to determine the crystal orientation of the sample.

Chapter 6

Results and discussion

In this chapter, the results from the laboratory experiments are being presented. Each section includes a discussion of the different result in relation to the theory presented in chapter 2 and to previous studies presented in chapter 4.

6.1 GaN:Mg substrate treatments

The GaN:Mg samples were activated with RTA using different recipes. The annealing process was done to get p-type conductivity in the GaN films. Some of the samples were also etched in a ICP-RIE system before or after the annealing process because p-type conductivity couldn't be confirmed only from RTA.

In table 6.1 the carrier concentration, the type of charge carriers and resistivity estimates for the different GaN samples are displayed. The values are found from Hall measurements. The first series of measurements are done after cleaning the GaN-samples and annealing them at different temperatures. The next series of measurements are done after cleaning, annealing and etching the samples. The last series in the table are done after cleaning, etching and then annealing the samples.

The highest carrier concentration of 1.22 x 10^{18} cm^{-3} resulted from RTA at 580 ° C using O_2 as the background gas. The process is similar to the RTA process reported in [47] which led to a carrier concentration of 2 x 10^{17} cm^{-3}. Because the number of charge carriers is important for the performance of a solar cell device, this process was chosen for the remaining samples. Unfortunately, all the samples activated using RTA showed n-type conductivity when expecting p-type. After etching a surface layer of $\sim$ 300 nm, the samples had lower carrier concentration and higher resistivity but

Table 6.1: Overview of the different pre-treatments with the resulting carrier concentration, type of charge carriers and resistivity estimates

Pre-treatment	Carrier concentration (cm^{-3})	Type	Resistivity (Ω-cm)
RTA 950 ° C N_2	1.3 x 10^{18}	p	0.0143
RTA 580 ° C O_2	1.532 x 10^{18}	p	0.0883
RTA 620 ° C O_2	1.22 x 10^{18}	p	0.290
Etching with ICP-RIE, RTA 580 ° C O_2	8.80 x 10^{17}	p	0.298
RTA 580 ° C O_2, Etching with ICP-RIE	6.66x 10^{17}	p	0.162

still showed n-type conductivity. This means that the etching process made the films worse independently of whether the Mg-activation took place before or after the ICP-RIE etch. This is consistent with what they report in [46], where introduction of N-vacancies caused by the RIE process made contacts to GaN worse.

The reason for the n-type conductivity after etching the samples could mean that the activation process chosen were unable to produce p-type GaN:Mg. This is not in agreement with what they observed in [47], but it is however reported that p-type GaN:Mg is difficult to achieve [17]. It could also be that the etching process were unable to remove all the unintentional Si. More experiments should be carried out to determine if other pre-treatments of the GaN:Mg wafer could lead to p-type conductivity.

6.1.1 Etching characteristics for the GaN:Mg wafers

Etching of the GaN-samples was done because there was a thin surface layer $\sim$ 100 nm that contained unintentional high background Si. Different recipes were tested to determine the etching rate of GaN. The recipes are displayed in table 5.2. Etching a sample for 10 minutes with 20 W Radio frequency (RF) power resulted in etching away the entire $\sim 7\mu$m GaN:Mg film. A second run, using 10 W RF power and 1 minute etching time gave an etching rate of 427 nm/min. The last run of 30 seconds with 20 W RF power resulted in an etch rate of 592 nm/min. This recipe was used for the remaining samples as it resulted in etching a $\sim$ 300 nm thin surface layer.

The etching characteristics was studied to see if the etching process degraded the surface layer or significantly changed the the ratio of Ga and N in the surface region. Figure 6.1 shows surface pictures of the GaN:Mg wafer before and after etch taken with the table top SEM.

It seems like the surface layer was not degraded by the etching process as the SEM picture taken after etching does not show any larger impurities or cracking compared to the SEM picture taken before the etching step.

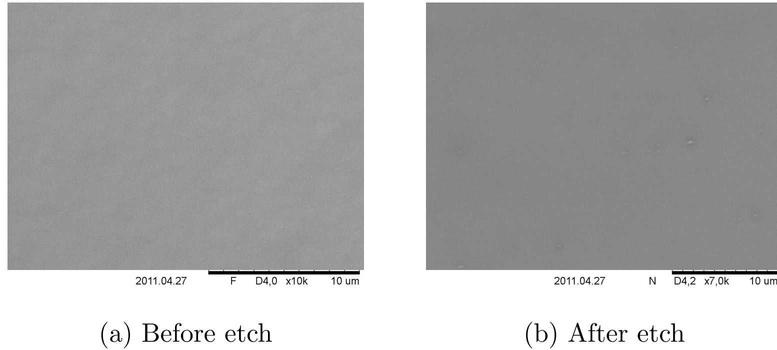

(a) Before etch (b) After etch

Figure 6.1: SEM surface pictures of the GaN:Mg wafer before and after etch

In table 6.2, the ratio of the different elements Ga, N, Al, O and C before and after etching of a GaN:Mg sample is displayed. The detection of Al and O arises from the sapphire substrate and oxygen at the sample surface, while carbon arises from surface contamination.

Table 6.2: EDX of a GaN:Mg sample before and after etching

Element	Concentration before etching [at. %]	Concentration after etching [at. %]
Ga	45.9	44.0
N	28.7	35.5
Al	7.1	3.0
O	0	4.6
C	18.3	13.0

The ratio between Ga and N were not significantly changed due to the ICP-RIE process so the etching seems to be uniform for the two elements and not changing the surface structure of the GaN wafer.

6.2 Thickness measurements of the ZnO:Co thin films

The thickness of the ZnO:Co films on sapphire substrate grown by PLD was measured using SEM cross section imaging and by using a profilometer. The high concentration films have two corners that were unexposed during the PLD growth due to the substrates being mounted mechanically to the substrate holder, so these films were measured using a profilometer. For the low concentration samples, the substrates were glued to the substrate holder,

so these films were investigated using SEM cross section imaging. In figure 6.2, the cross section images for the 1, 2 and 5 % Co concentration films are presented. Table 6.3 displayes the thickness determined for all the samples.

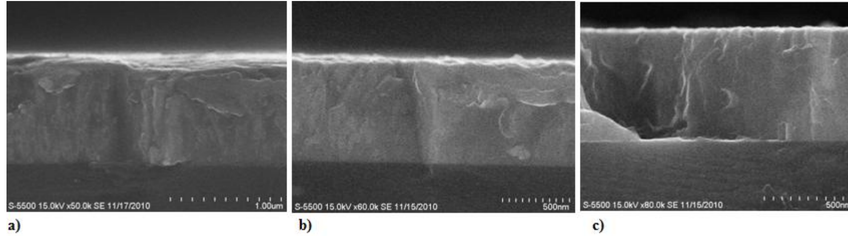

Figure 6.2: Cross section images of the a) 1 %, b) 2 % and c) 5 % Co sample.

Table 6.3: Thickness measurements of the ZnO:Co samples on sapphire substrates

Sample	Thickness [nm]
1 % Co	1000
2 % Co	700
5 % Co	600
10 % Co	290
20 % Co	250
30 % Co	190

The deposition duration were about the same for all the films, so this suggest that the growth rate decreases with increasing cobalt concentration. This is the same as what the observed in [62], where ZnO:Co films grown in low oxygen pressure or vacuum resulted in thinner films with higher Co concentration.

6.3 Dark I-V measurements to determine contact quality of the ZnO:Co and GaN:Mg semiconductor thin films

From the Hall measurements setup, dark I-V curves were recorded for all the ZnO:Co and GaN:Mg films. For the ZnO:Co films with various cobalt doping concentration, the result showed linear I-V curves from all the Ti/Au contact

pairs, which indicates good ohmic contact to the semiconductor surface. This is consistent with what they report in the literature [49] [50]. Figure 1 shows the IV curves recorded for the 1 % Co film for all the contact pairs 12, 23, 34 and 41.

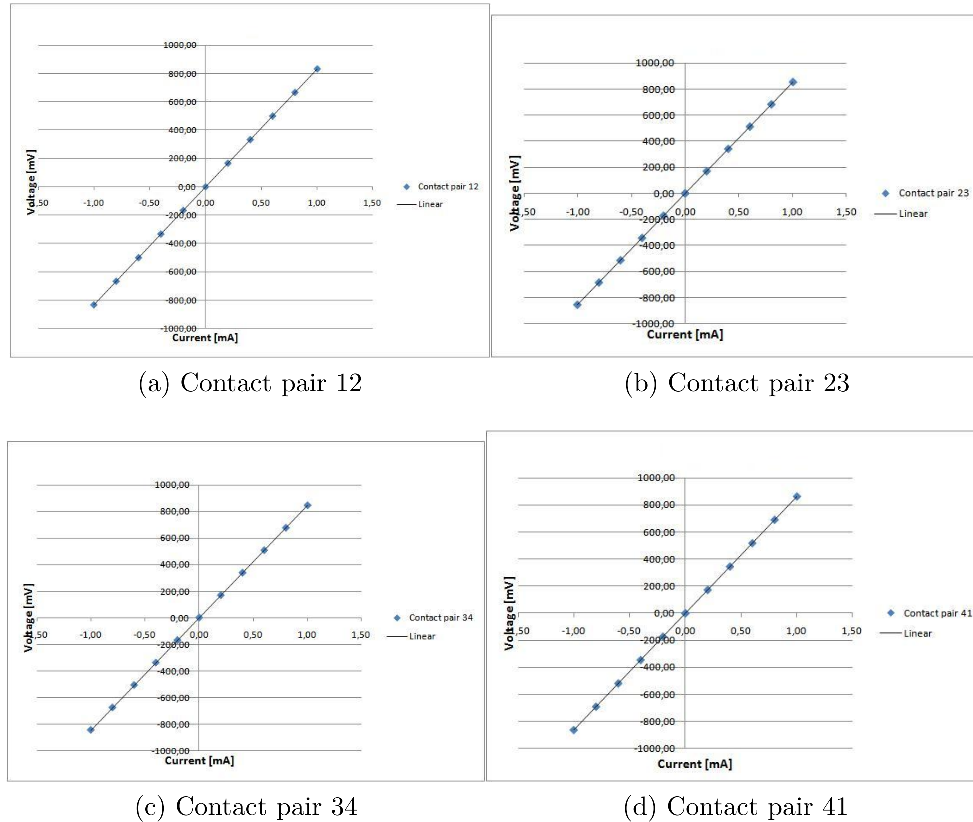

(a) Contact pair 12

(b) Contact pair 23

(c) Contact pair 34

(d) Contact pair 41

Figure 6.3: IV curves recorded for the 1 % Co film for all the contact pairs 12, 23, 34 and 41

Similarly, I-V curves were recorded for the preliminary contacts made with InGa to the GaN:Mg activated thin films. Here, it is evident that the metal contacts don't have the same quality as the contacts to ZnO:Co as the I-V curves tend to be somewhat s-shaped instead of linear. This indicated a Schottky barrier between the metal/semiconductor interface [53]. Figure 2 shows the IV curves recorded for the GaN:Mg film activated at 580 ° C in oxygen ambient for all the contact pairs 12, 23, 34 and 41.

From the figure, some of the contact pairs have the desired linearity, while others do not. It is not clear why some of the contacts are better than others, but factors such as the positioning and finite area of the contacts may play

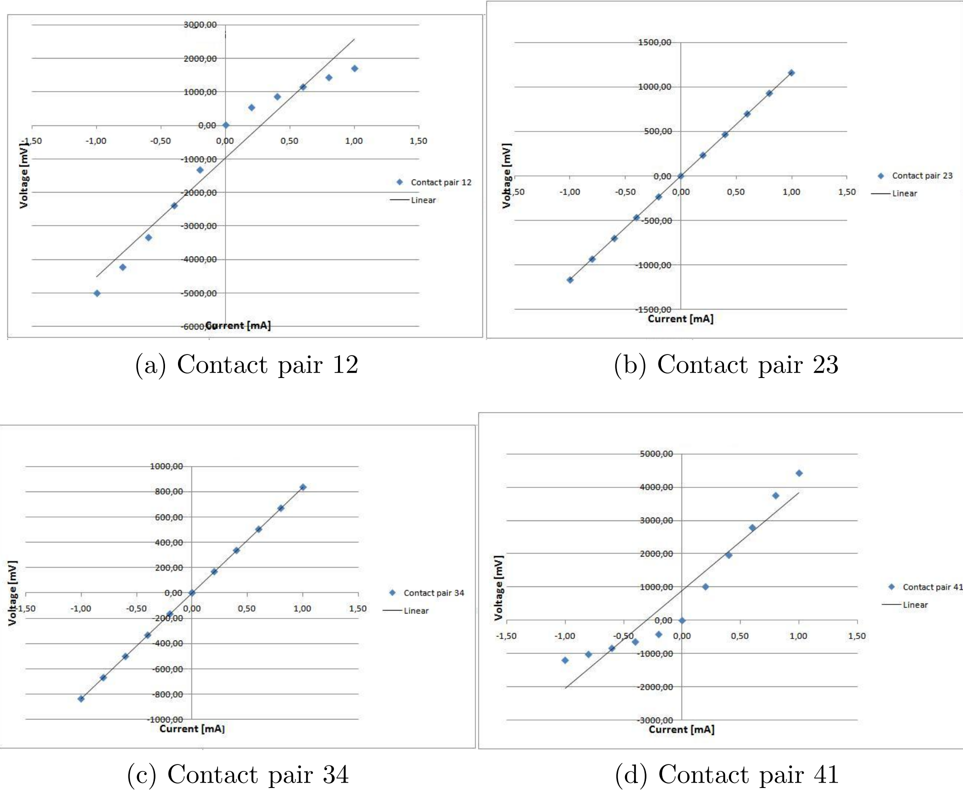

(a) Contact pair 12

(b) Contact pair 23

(c) Contact pair 34

(d) Contact pair 41

Figure 6.4: IV curves recorded for the GaN:Mg film activated at 580 ° C for all the contact pairs 12, 23, 34 and 41

a role. Surface states in the Mg:GaN also affect the properties of the M-S contact as discussed in section 2.3.3.

To find the average value of the contact resistance of the Ti/Au and InGa contacts, equation (2.23) was used. The total resistance R_T is found by calculating the slopes from the figures 6.3 6.4, while the semiconductor resistance R_s is found from Hall measurements. The result is an average contact resistance of R_c= 496 Ω for the Ti/Au contacts and R_c= 1702 Ω for the InGa contacts. The higher resistance for the InGa contacts is a result of the Schottky barrier indicated in figure 6.4a and 6.4d

6.4 Hall measurements to determine carrier concentration and resistivity estimates for the ZnO:Co thin films

Resistivity estimates from Hall measurements of the different cobalt doped ZnO thin films deposited on sapphire are presented in table 6.4 together with the carrier concentration for each sample. Table 6.5 shows resistivity estimates calculated for the same films using a four-point-probe measurement system.

Table 6.4: Resistivity estimates from Hall measurements

Sample	Resistivity (Ω-cm)	Carrier concentration (cm^{-3})	Type
1 % Co	0.012	3.56 x 10^{19}	n
2 % Co	0.012	5.88 x 10^{19}	n
5 % Co	0.021	1.31 x 10^{18}	n

Table 6.5: Resistivity estimates from four-point probe measurements

Sample	Resistivity (Ω-cm)
1 % Co	0.286
2 % Co	0.260
5 % Co	0.097

The high concentration samples containing 10, 20 and 30 % cobalt were also measured in the Hall measurement system, but these samples were isolating with a resistance of >GΩ, so the resistivity and carrier concantration could not be determined for these samples. The increase in resistivity with increasing doping concentration from the Hall measurements is consistent with what they report in the literature [36] [28]. All the samples shows n-type conductivity, which is as expected for Co-doped ZnO [36]. The values for the resistivities are in the range of what they reported in [63], where a bulk ZnO sample containing 1 % Co has a resistivity of 0.049 Ω-cm.

The resistivity from the four-point-probe measurements is higher than from Hall measurements, and the resistivity seems to decrease with higher doping concentration. The reason for the high resistivity could be because

the probes were applied directly to the ZnO:Co surface without any metal contacts. This could result in non-ohmic contact or high contact resistivity between the ZnO:Co surface and the probes. The reason for the decrease in resistivity with higher doping concentration in this setup is not clear, but the currents that could be driven through the samples were very small, ~20-40 μA, so the large resistance in the circuit will contribute to large uncertainties in the measurements.

The carrier concentration varies from $\sim 10^{19}$ cm^{-3} in the 1 and 2% Co concentration film to $\sim 10^{18}$ cm^{-3} for the 5 % Co concentration film. The values are in the range of what is observed for n-type ZnO [44]. The relationship between ther carrier concentration n, resistivity ρ and electron mobility μ is given by [19]

$$\mu = \frac{1}{\rho n e} \tag{6.1}$$

From this, the electron mobilities are calculated to be 18, 8.85 and 227 cm^2/(V s) for the 1, 2 and 5 % cobalt samples. In [64] they reported similar values ~ 20 cm^2/(V s) for the mobility in ZnO samples containg 0, 4 and 25 % cobalt.

6.5 Optical properties of the ZnO:Co thin films

The optical properties of the ZnO:Co was studied using optical transmission spectroscopy. Figures 6.5, 6.6 and 6.7 shows the optical transmission spectra for the ZnO:Co thin films recorded with the ThorLabs Compact fiber spectrometer.

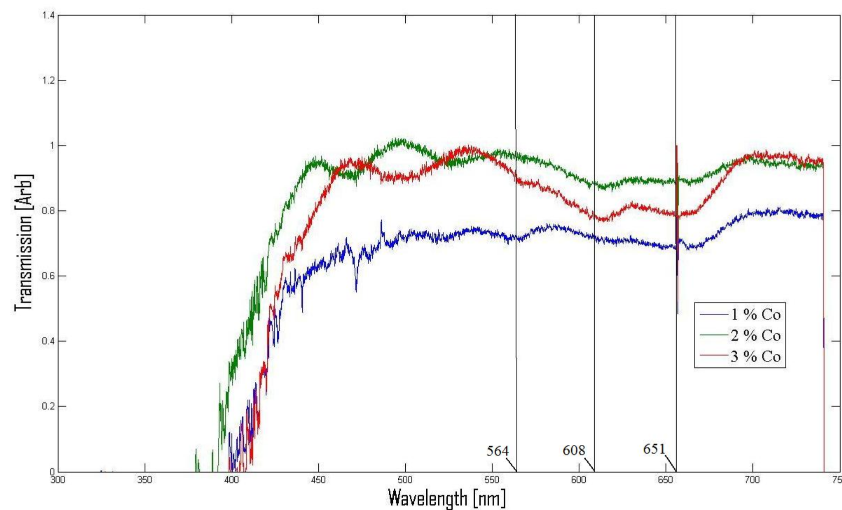

Figure 6.5: Transmission spectra for the 1, 2 and 5 % cobalt doping concentration samples.

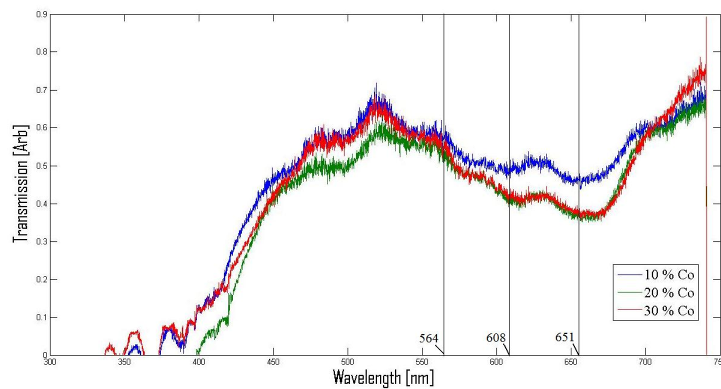

Figure 6.6: Transmission spectra for the 10, 20 and 30 % cobalt doping concentration samples.

All the spectra shows absorption lines at certain wavelengths, but the lines are difficult to identify because of fringes in the spectra. Initially, the fringes

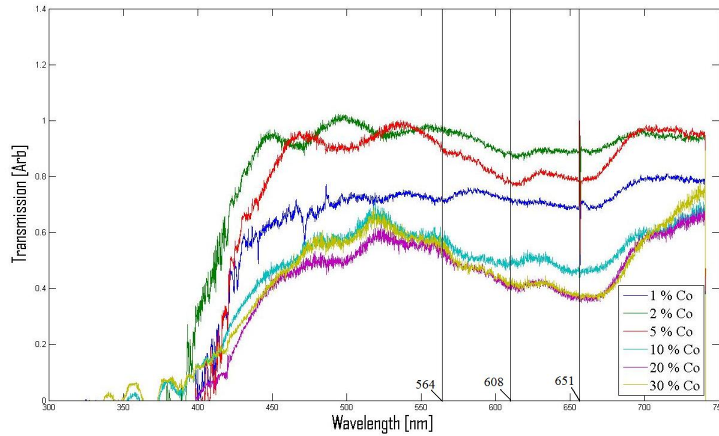

Figure 6.7: Transmission spectra for the 1, 2, 5, 10, 20 and 30 % cobalt doping concentration samples.

were believed to be due to interference between the sapphire substrate and the ZnO:Co thin film, but when the films were remeasured using a different spectrometer, an AvaSpec from Avantes, the fringes disappeared and three absorption lines could be identified. For this reason it was concluded that the fringes caused by the ThorLabs Compact fiber spectrometer was an artifact of the instrument. Figure 6.8 shows the transmission spectra for the high concentration samples using the AvaSpec spectrometer. The absorption lines are marked in the figure. From the theory, the absorption lines arises from characteristic d-d transition levels attributed to Co^{2+} occupying tetrahedral lattice positions indicating that cobalt is substituting as Co^{2+} on Zn lattice sites. The lines should be located at energies of 1.9 eV (651 nm), 2.0 eV (608 nm) and 2.2 eV (564 nm) [35]. These values are very close to the values found from the new transmission spectra, which indicates that Co^{2+} is substituting for Zn in the Co-doped thin films.

The theoretical values of the absorption lines are also marked in the figures 6.5, 6.6 and 6.7.

Because the datapoints could not be extracted from the new transmission spectra due to the software not being able to export data, the rest of the discussion in this section relates to figures 6.5, 6.6 and 6.7.

In figure 6.5 the spectra for the 1, 2 and 5 % Co concentration samples are displayed. The theoretical band gap of pure ZnO is located at 370 eV. All the low concentration samples seems to have a band gap that is not significantly different from this theoretical value. The absoption lines seems to increase with Co contents, and for the 1 % Co samples almost no absoption can be identified.

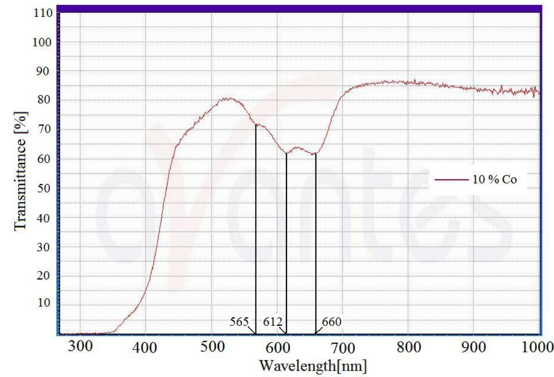

(a) 10 % Co concentration sample.

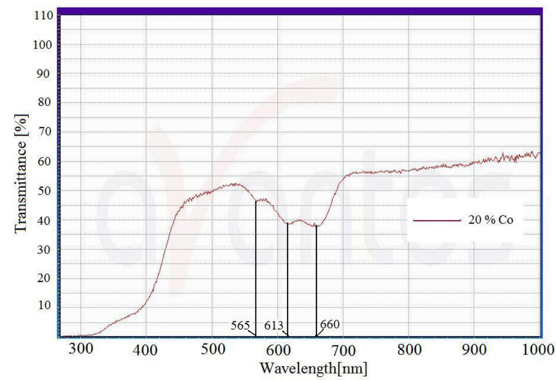

(b) 20 % Co concentration sample.

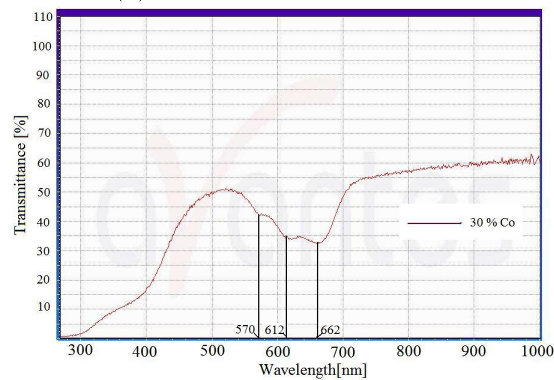

(c) 30 % Co concentration sample.

Figure 6.8: Transmission spectra for the high concentration samples using the AvaSpec spectrometer.

In figure 6.6 the spectra for the 10, 20 and 30 % Co concentration samples are displayed. With increasing Co content, the absorption edges are red shifted. This change in E_g with Co is explained by sp-d exchange interactions between the band electrons in ZnO and localized d electrons of Co^{2+} [29]. In

[29], they observed the same phenomenon, where E_g decreased from 3.27 to 2.88 eV with increasing Co contant from x = 0 to x = 0.15 in $Zn_{1-x}Co_xO$.

In figure 6.7 all the spectra are plotted in the same graph. The overall transmission throughout the visible range is lower for the high concentration samples. This may be due to the reduced transparency of the film, as the films are increasingly more green colored due to the cobalt doping. The green color is assigned as typical d-d transitions of high spin states Co^{2+} $3d^7(^4F)$ in a tetrahedral oxygen configuration [29]. It is also clear that the absorption lines are stronger for the high concentration thin films. This may suggest that when increasing the cobalt concentration, more cobalt is substituting as Co^{2+} on Zn lattice sites and not forming metallic clusters of cobalt.

To examine the absorption due to characteristic Co^{2+} transitions the absorption coefficient α as a function of cobalt concentration at 652 nm was plotted. Figure 6.9 displays the result for all the samples. The absorption coefficient is calculated according to equation (4.1).

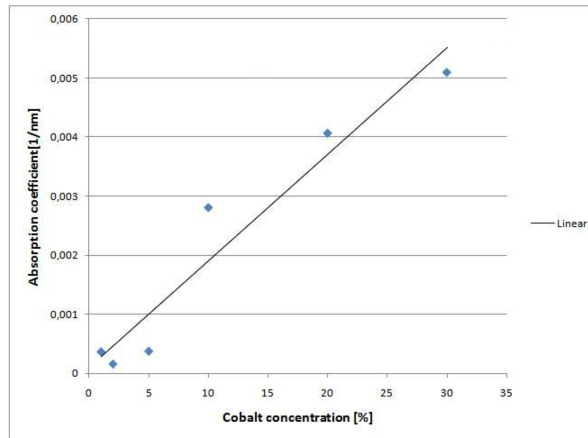

Figure 6.9: Absorption coefficient as a function of cobalt doping concentration

From the figure, a nearly linear relationship between the cobalt concentration and absorption coefficient can be observed. This is in agreement with what they observed in [35], where the absorption coefficients for the different films containing 0, 2, 10, 15 and 30 % cobalt were calculating by taking the area underneath the characteristic absorption wells from Co^{2+} transitions of the transmission spectra. The linear relationship between the absorption coefficient and the cobalt concentration suggests that the cobalt is dissolved in the ZnO lattice.

The bandgap of the doped ZnO films was determined by using Tauc plots [35]. The absorption coefficient α for a direct interband transition is given

by [33]

$$\alpha h\nu = B(h\nu - E_g)^2 \tag{6.2}$$

where B is the slope of Tauc edge called the band tailing parameter. B depends on the width of localized states in the band gap. The band gap was calculated by plotting $(\alpha h\nu)^2$ as a function of $h\nu$ and extrapolating the linear part of the plot to $(\alpha h\nu)^2 = 0$. The plots are given in figure 6.2.

The bandgap lies close to 3.1 eV for all the plots, but there is a shift towards lower energies especially for the high concentration films. This is in agreement with what they observed in [29], where the Tauc plot showed a decrease in E_g from 3.27 to 2.88 eV with increasing Co content from 0 to 15 %.

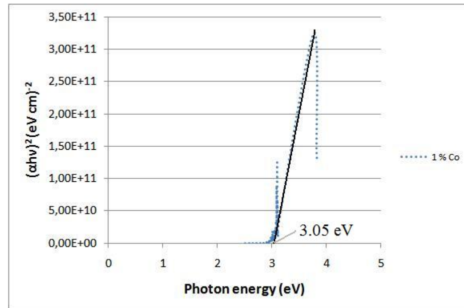

(a) Plot of $(\alpha h\nu)^2$ versus $h\nu$ for 1 % Co film.

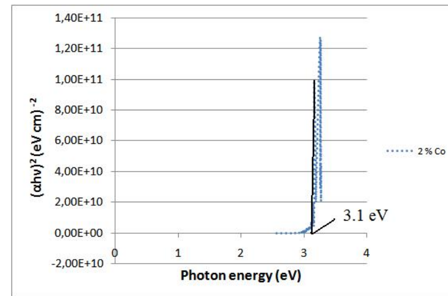

(b) Plot of $(\alpha h\nu)^2$ versus $h\nu$ for 2 % Co film.

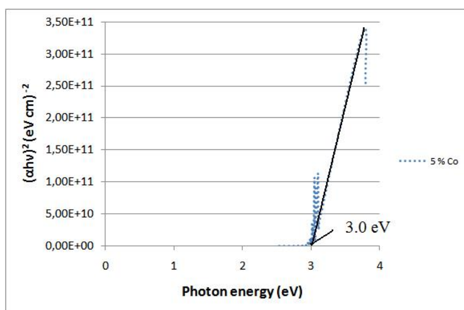

(c) Plot of $(\alpha h\nu)^2$ versus $h\nu$ for 5 % Co film.

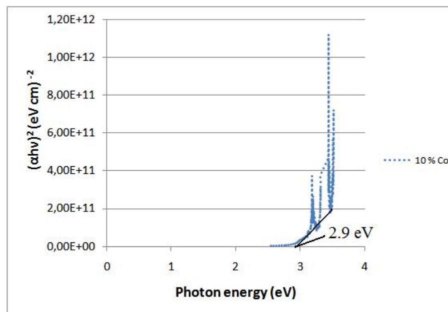

(d) Plot of $(\alpha h\nu)^2$ versus $h\nu$ for 10 % Co film.

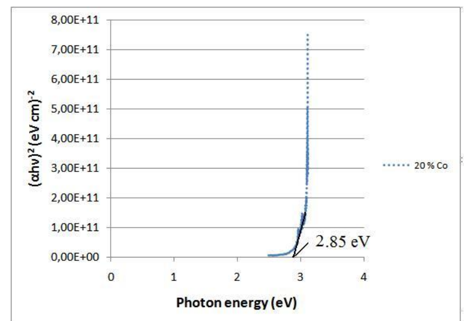

(e) Plot of $(\alpha h\nu)^2$ versus $h\nu$ for 20 % Co film.

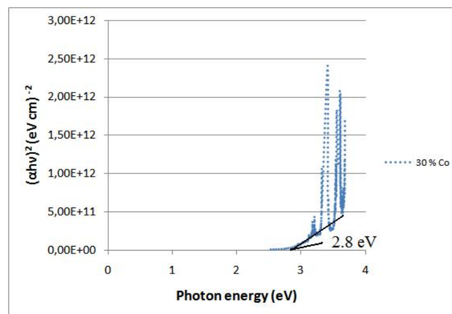

(f) Plot of $(\alpha h\nu)^2$ versus $h\nu$ for 30 % Co film.

Figure 6.10: Optical bandgap plots for Co-doped ZnO films

6.6 Determination of the crystal-orientation in the ZnO:Co thin films

XRD was used to determine the crystal-orientation in the ZnO:Co thin films. $\theta - 2\theta$ scans were run on all the samples (from 1% to 30 % Co concentration). Figure 6.11 shows $\theta - 2\theta$ scans for the samples containing 10, 20 and 30 % Co. The low concantration samples show the same ZnO intensity peaks.

From the figure, intensity peaks corresponding to sapphire(006), ZnO(002) and ZnO(004) are detected. Because the spectra only shows ZnO (00n) reflections in addition to the substrate peak, this means that the films has the same c-orientation as the substrate. This is consistent with what they reported in [35] [41] where thin films of ZnO:Co grown by PLD were investigated by XRD. The sapphire(006) peak is narrow while the ZnO(002) and ZnO(004) peak are broader. This suggests that the substrate has perfect c-orientation while the crystal structure of the ZnO:Co films are c-oriented with reasonable order. From the literature [35] they observe the same broadening of the ZnO(00n) peaks compared to the sapphire(00n) peaks concluding that the films are predominately c-oriented. No additional peaks indicating cobalt metal precipitation was detected from the $\theta - 2\theta$ scans.

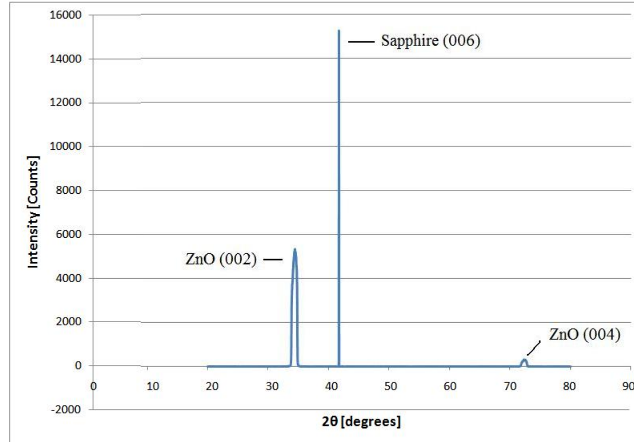

(a) 10 % Co concentration sample.

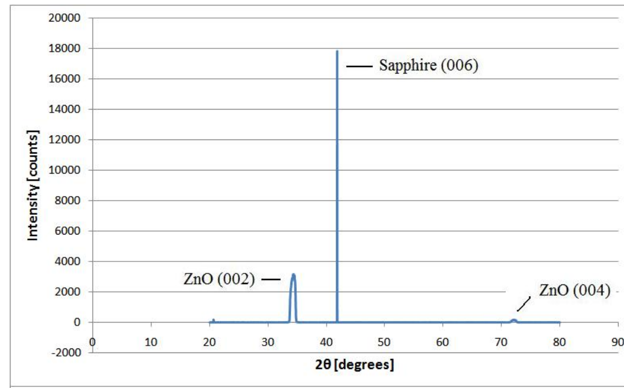

(b) 20 % Co concentration sample.

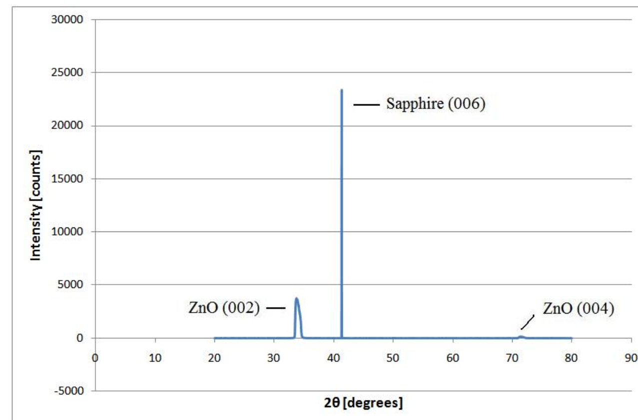

(c) 30 % Co concentration sample.

Figure 6.11: θ - 2θ curves for the high concentration samples.

6.7 Chemical composition

XPS was used to determine the chemical composition of the low concentration films. The data includes measurements of the series of low concentration films deposited on sapphire together with a series of low concentration films deposited on silicon.

Figure 6.12 shows the survey spectrum for the 2 % Co sample deposited on silicon. The intensity peaks investigated are marked on the figure. To determine the chemical composition of Zn, O and Co in the samples, the area under the intensity curves is used after subtracting the background from the spectrum. For calibration, the O 1s orbital peak is aligned at 530.2 eV, which is a typical binding energy reported for the O 1s peak in ZnO [35].

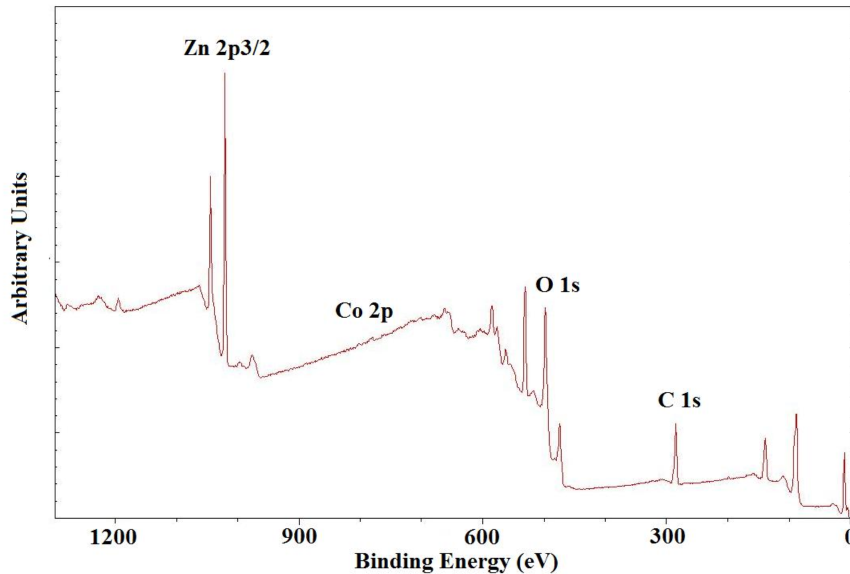

Figure 6.12: Survey spectrum of the 2% Co sample deposited on silicon.

Table 6.6 shows the atomic percentage of zinc, oxygen and cobalt of the samples deposited on silicon from the XPS measurements. The atomic concentration of cobalt increases with increasing doping, as one should expect. The values of Co compared with the ones for Zn seems to be in the right order of magnitude for the three different samples, although the cobalt concentration of the 1 % sample was too low to compare with the oxygen and zinc in the sample. The high level of oxygen for all the samples is due to oxygen absorption on the surface of the samples. Since XPS is a surface analyze technique, it will be sensitive to this process. There is also additional surface contamination of carbon. To reduce the surface contamination to get

higher intensities from the Zn and Co, the films could have been sputtered with Ar^+ ions as reported in previous studies [35].

Table 6.6: Chemical composition of the samples on silicon from the XPS measurements.

Sample	Zn (at %)	O (at %)	Co (at %)
1 % Co	-	-	Too low concentration
2 % Co	18.4	81.4	0.26
5 % Co	17.5	81.0	1.48

Figure 6.13 shows a high resolution energy spectrum from the Co 2p orbital for the six samples investigated. The intensity of the peaks should increase with higher doping concentration. The intensity for the two samples with lowest concentration seems to be lower than for the other samples, but there is no significant change in the intensity between the 2 % and 5 % Co samples.

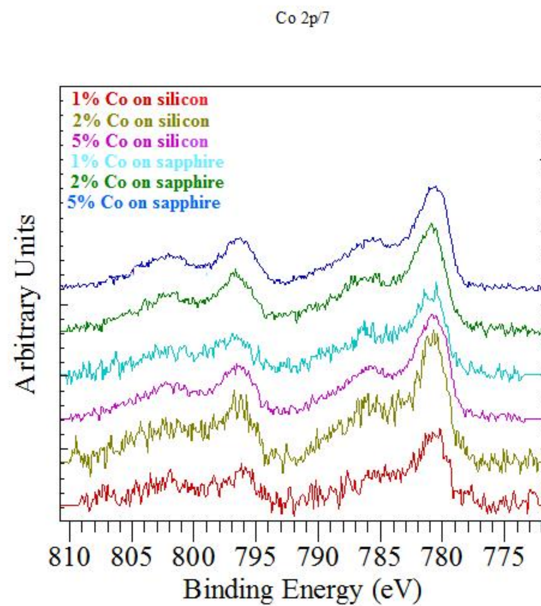

Figure 6.13: High resolution energy spectrum of the samples.

The high resolution spectra can also be used to determine the valance state of the cobalt in the samples. The $2p_{3/2}$ peak located at 780.5 eV is due to the Co $^{2+}$ oxidation state[35]. The energy separation between the $2p_{3/2}$

and $2p_{1/2}$ is about 15.6 eV, which is more consistent with Co in CoO, with a value of 15.2 eV [65], than in metallic cobalt, with a value of 14.97 eV [65].

6.8 Device fabrication using ZnO:Co as intermediate band material

Because the GaN:Mg wafer did not show p-type conductivity, the fabrication of a p-IB-n device was not done. Instead, Schottky diodes of M-ZnO:Co were made to be able to study the photoresponse of the ZnO:Co thin films. Both Au and Pt contacts were deposited on the ZnO:Co surface, and dark I-V curves were recorded for the different configurations.

Figure 6.14 shows dark I-V curves recorded for the Au-ZnO:Co and Pt-ZnO:Co Schottky diodes. They both show linear I-V characteristics independent of the direction of the applied voltage. Both Au and Pt are expected to form a Schottky barrier to n-type ZnO because of the high metal work functions for these materials [53] [54] [57] [56], but the linear characteristics indicates ohmic contacts.

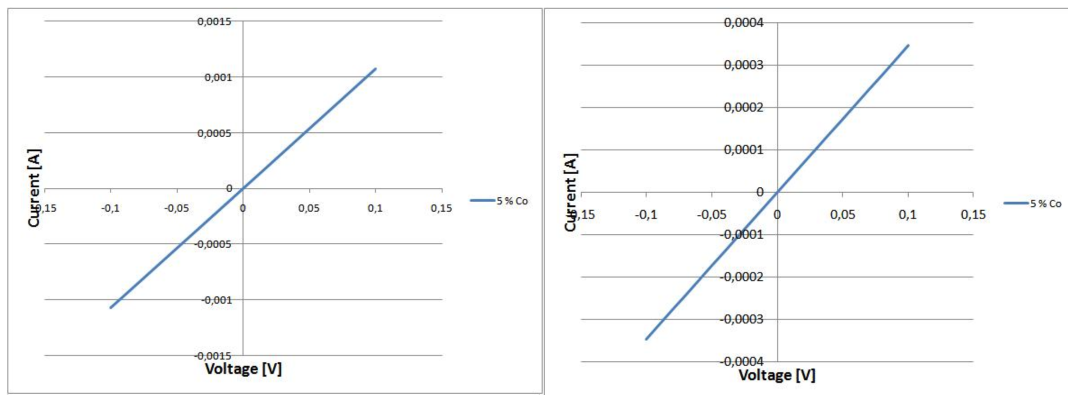

(a) Schottky Au contact

(b) Schottky Pt contact

Figure 6.14: Dark I-V curves for M-ZnO:Co Schottky diodes

To see if any diode behavior could be identified at all, the region around I=0, V=0 was investigated for the Pt-ZnO:Co Schottky diode. Figure 6.15 shows dark I-V curves for the Pt-ZnO:Co Schottky diode for voltages in μV range. When decreasing the voltage, a jump in the slope around I=0 can be observed independent of the direction of the applied voltage.

Possible circuit configurations were investigated to explain the jump in the slope. Figure 6.16 shows two different configuration investigated.

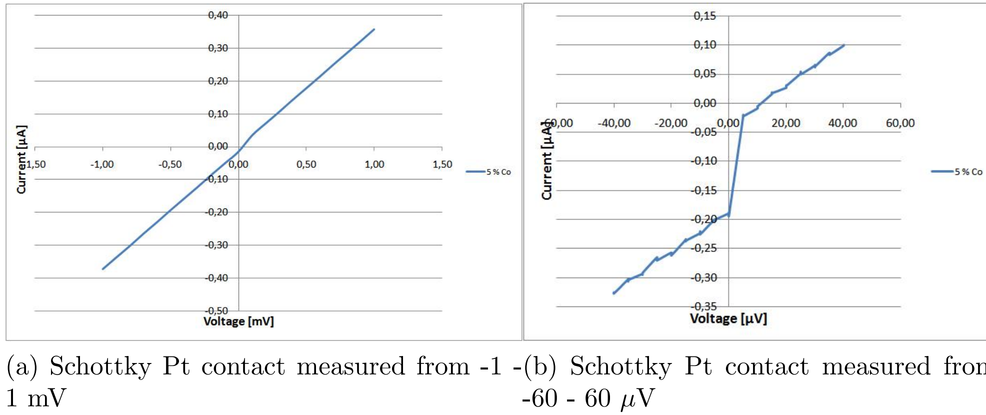

(a) Schottky Pt contact measured from -1 - 1 mV

(b) Schottky Pt contact measured from -60 - 60 μV

Figure 6.15: Dark I-V curves for Pt-ZnO:Co Schottky diodes for decreasing voltages

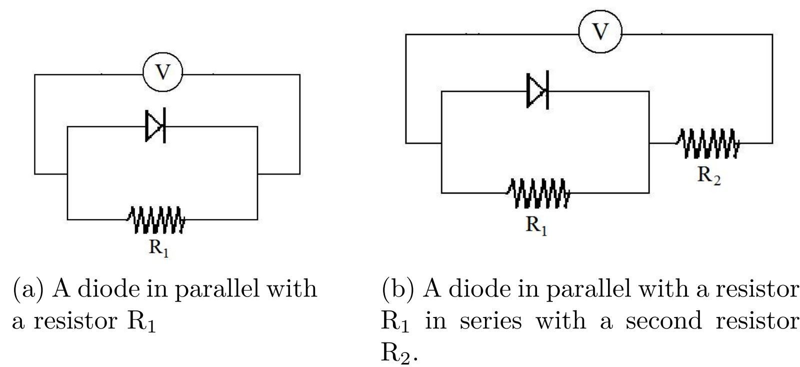

(a) A diode in parallel with a resistor R_1

(b) A diode in parallel with a resistor R_1 in series with a second resistor R_2.

Figure 6.16: Possible circuit configurations for the M-ZnO:Co Schottky diodes.

In figure 6.16a, the diode is placed in parallel with resistor R_1. If it has a large resistance, the diode would be shorted when the voltage is applied in the forward direction while the resistor would act as a linear resistance in the reversed direction. This configuration cannot explain the I-V characteristics from the figures given above as it would show diode characteristics in one direction.

In figure 6.16b, the diode is placed in parallel with resistor R_1 in series with a second resistor R_2. If $R_1 \gg R_2$, there would be a linear resistance R_2 in the forward direction in addition to the diode behavior, while in the reversed direction, a linear resistance equal to $R_1 + R_2$ would be observed. This would give rise to a change in the slope at V=0. A plot of the linear part of figure 6.15a for positive and negative voltages independently is shown in

figure 6.17. The value of the slope is exactly the same in each region which means that the observed I-V characteristic cannot be explained by circuit configuration in figure 6.16b.

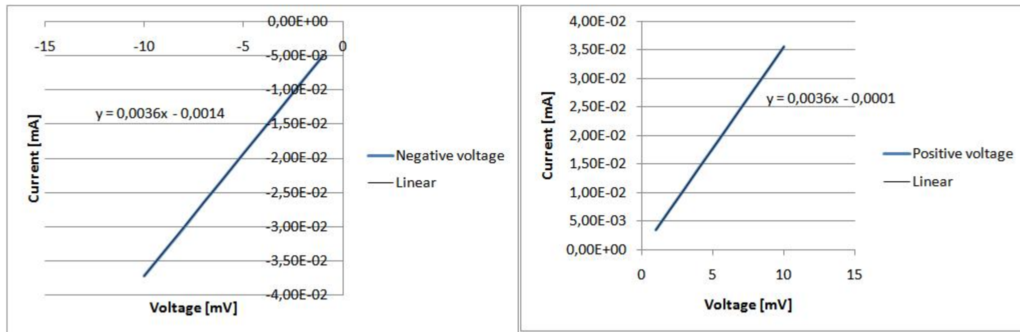

(a) Negative voltage (b) Positive voltage

Figure 6.17: Plot of the linear part of figure 6.15a for positive and negative voltages.

Probably, the sudden jump in the slope around I=0 is an artifac of the measurements setup. The accuracy of the setup is limited to measure currents and voltages in μA and μV range [60], so the I-V characteristics close to I=0, V=0 cannot be determined properly.

The reason for the ohmic behavior of Pt contacts to ZnO:Co is explained in [66] by high donor concentration at the surface region of n-ZnO which is caused by defects of oxygen vacancies and zinc interstitials. They report that conventional cleaning in organic solvents did not result in Schottky contacts. Instead they used an additional sulfide treatment consisting of boiling the samples in $(NH_4)_2S_x$ solution for 30 seconds before deposition of the Pt contacts. This lead to a rectifying I-V characteristic indicating a Schottky barrier. The formation of the Schottky barrier is explained in [66] by selfcompensation in ZnO because the surface region of the sulfide-treated ZnO contains donor concentrations lower than that of the bulk ZnO. In addition, the interfacial ZnS layer has low conductivity [66] so these combined effects could be responsible for the formation of good Pt Schottky contacts to sulfide-treated ZnO surfaces. Investigating additional surface treatments before deposition of Schottky contacts to ZnO:Co should be done to be able to get the desired Schottky properties.

Chapter 7

Conclusion and future work

In this thesis, epitaxial ZnO:Co were deposited by PLD over a large concentration range. Characterization techniques including Scanning Electron Microscopy (SEM), Energy Dispersive X-ray (EDX) Microanalysis, X-ray Photoelectron Spectroscopy (XPS), Hall measurements, X-ray diffraction (XRD) and optical transmission spectroscopy was used to investigate the properties of the deposited films. Optical transmission and XPS showed that the cobalt in the ZnO:Co films were mostly in a $^{2+}$ state, indicating that Co is substituting for Zn in the ZnO lattice. XRD showed the crystal structure to be epitaxial with reasonable order. Metallic phases of cobalt were not detected from XPS and XRD. The carrier concentration in the ZnO:Co films were in the order of 10^{18}- 10^{19}, decreasing with increasing cobalt concentration. The resistivity in the samples increased with increasing doping concentration.

The GaN:Mg wafer investigated did not have the desired properties for device fabrication as it showed n-type conductivity when expecting p-type. The Schottky diodes made of Au-ZnO:Co and Pt-ZnO:Co did not show diode behavior because of surface states in ZnO:Co making ohmic contacts to the metals.

To continue the research presented in this thesis, the fabrication of a p-IB-n or a Schottky device using the ZnO:Co as the IB material is needed. This will allow for investigation of the photoresponse in the material and may give an indication of the existence of an intermediate band. A p-type semiconductor material should be properly made, i.e. by investigating additional pre-treatments of GaN:Mg. For the Schottky devices, additional surface treatments of the ZnO:Co should be investigated to be able to make Schottky diodes with the desired I-V characteristics.

Appendix A

PLD parameters

Table A.1: Overview of samples deposited by PLD including all the parameters used

Sample ID	ZC110201	ZC110301	ZC110302	ZC110401
Substrate	p-Si(001)	c-sapphire	c-sapphire	c-sapphire
Target	ZnO:Co(10%)	ZnO:Co(10%)	ZnO:Co(20%)	ZnO:Co(30%)
Dep. duration[min]	67	65	60	60
Slit[mm^2](x+x)*(z+z)	(2+2)(4+4)	(2+2)(4+4)	(2+2)(4+4)	(2+2)(4+4)
Attenuator position	850	850	840	855
After optics [W]	0.21	0.21	0.20	0.21
IV power meter [W]	0.07	0.06	0.07	0.07
Power on the target [W]	0.1575	0.135	0.1575	0.1575
Pulse energy [mJ]	1520	1520	1520	1520
Laser pressure[mbar]	3274	3281	3269	3245
T setpoint [°C]	450	450	450	450
T-S distance	45	45	45	45
Heater[V]	7	8.3	8.2	7.6
Heater[A]	8	8.5	8.1	8
Gas pressure[mbar]	1 x 10^{-2}	1^{-2}	1^{-2}	1^{-2}
Base pressure[mbar]	4 x 10^{-7}	4 x 10^{-7}	4 x 10^{-7}	4 x 10^{-7}
Gas mixture(oxygen/argon)[%]	(100/0)	(100/0)	(100/0)	(100/0)
Target scan area	12mm (round)	12mm (round)	12mm (round)	12mm (round)
Spot size(w/h)	(1/2)	(1/2)	(1/2)	(1/2)
Scan speed(pre/dep)	100	100	100	100
Laser pulse rep. rate [Hz]	10	10	10	10

Bibliography

[1] *Renewable Energy Resources*, J. Twidell and T. Weir, Taylor & Francis (2006)

[2] *Key World Energy Statistics 2010*, International Energy Agency (2010)

[3] *The Intermediate Band Solar Cell: Progress Toward the Realization of an Attractive Concept*, A. Luque et al., Advanced Materials **22**, 160-174 (2010)

[4] *Solar Cells, Operating Principles, Technology and System Applications*, M. A. Green (1998)

[5] *Theoretical studies of the intermediate band solar cell*, Rune Strandberg, Doctoral theses at NTNU, (2010)

[6] *Present status of intermediate band solar cell research*, L.Cuadra et al., Thin Solid Films 451-452, 593-599 (2004)

[7] *Increasing the efficiency of ideal solar cells by photon induced transitions at intermediate levels*, A. Luque, A. Marti, Physical Review Letters **78**, 5014-17, (1997)

[8] *Handbook of photovoltaic science and engineering*, A. Luque and S. Hegedus, Wiley (2003)

[9] *The physics of solar cells*, J. Nelson, Imperial College UK (2002)

[10] *Application of the photoreflectance technique to the characterization of quantum dot intermediate band materials for solar cells*, E. Cánovas et al., Thin Solid Films 516 (2008)

[11] *Production of Photocurrent due to Intermediate-to-Conduction-Band Transitions: A Demonstration of a Key Operating Principle of the Intermediate-Band Solar Cell*, A. Marti et al., Physical Review Letters **97**, 247701 (2006)

[12] *A molecular approach to the intermediate band solar cell: The symmetric case*, N. J. Ekins-Daukes et al., Applies Physics Letters **93**, 063507 (2008)

[13] *Intermediate bands versus levels in non-radiative recombination* , A. Luque et al., Physica **B** 382, 320-327 (2006)

[14] *Analysis of metallic intermediate-band formation in photovoltaic materials*, C. Tableroa et al., Applies Physics Letters **82**, (2003)

[15] *Ab initio electronic structure calculations for metallic intermediate band formation in photovoltaic materials*, P. Wahnón ei al., Physical Review **B 65**, 165115 (2002)

[16] *Intermediate-band photovoltaic solar cell based on ZnTe:O*, W. Wang et al., Applied Physics Letters **95**, 011103, (2009)

[17] *Investigation of Contact Metallization for GaN Devices; Fabrication and Measurements of GaN SAW Resonator*, Sverre Vegard Pettersen, Doctoral theses at NTNU (2007)

[18] *Surface States and Rectification at a Metal Semi-Conductor Contact*, J. Bardeen, Physical Review, 71/10 717-727 (1947)

[19] *Understanding Solids, The Science of Materials*, R. Tilley, J. Wiley & sons, Ltd (2004)

[20] *Pulsed laser vaporization and deposition*, P. R. Willmott et al., Reviews of Modern Physics **72**, No.1, (2000)

[21] *NTNU NanoLab, SEM introduction course*, Powerpoint presentation, www.ntnu.no/nanolab

[22] *Scanning electron microscopy: physics of image formation and microanalysis*, Ludwig Reimer, Springer (1998)

[23] *Casa XPS Manual, 2.3.15 Introduction to XPS and AES*, N. Fairley, Casa software Ltd (2009)

[24] *Surface analysis with x-ray photoelectron spectroscopy - An introuction*, Powerpoint presentation, S. Diplas, SINTEF Oslo

[25] *X-ray photoelectron spectroscopy (XPS) for catalysts characterization*, A. M. Venezia, Catalysis Today **77**, 359-370 (2003)

[26] *Hansbook of Materials Measurement Methods*, Czichos, Saito and Smith, Ch. 11, Springer (2006)

[27] *Handbook of Semiconductor Interconnection Technology* Second Edition, Geraldine Cogin Schwartz, K.V. Srikrishnan, Arthur Bross, Geraldine C. Schwartz, Kris V. Srikrishnan, Taylor & Francis (2006)

[28] *Spectroscopy of Photovoltaic and Photoconductive Nanocrystalline Co2+-doped ZnO Electrodes*, X.C. et al., J. Phys. Chem. **B 109**, 14486 (2005)

[29] *Structural, optical and magnetic properties of Co-doped ZnO films*, X.C. Liu et al., Journal of crystal Growth 296 135-140 (2006)

[30] *Structural, optical and electrical properties of ZnO films grown by pulsed laser deposition (PLD)*, J. L. Zhao et al., Journal of Crystal Growth **276**, 507-512 (2005)

[31] *The structure and optical properties of ZnO nanocrystals dependence on Co-doping levels*, S. Wang et al., Journals of Alloys and Compound **505**, 362-366 (2010)

[32] *A comprehensive review of ZnO materials and devices*, Ü. Özgür et al., Journal of Applied Physics **98**, 041301 (2005)

[33] *Influences of Co doping on the structural and optical properties of ZnO nanostructured*, M. A. Majeed Khan et al., Applied Physics **A 100**, 45-51 (2010)

[34] *Optical and electrical properties of undoped ZnO films*, Y.J. Lin ei al., Journal of Applied Physics **99**, 093501 (2006)

[35] *Structure and magnetism of cobalt-doped ZnO thin films*, M. Ivill et al., New Journal of Physics **10**, 065002 (2008)

[36] *Cobalt-doped ZnO - a room temperature dilute magnetic semiconductor*, C. B. Fitzgerald et al., Applied surface science **247**, 493-496 (2005)

[37] *Magnetic semiconductors based on cobalt substitutes ZnO*, O. Durand et al., Journal of Applied Physica, 93/10 (2003)

[38] *The role of Zn interstitials in cobalt-doped ZnO diluted magnetic semiconductors*, T. Shi et al., Applied Physics Letters **96**, 211905 (2010)

[39] *Study of room temperature ferromagnetism for cobalt and manganese doped ZnO diluted magnetic semiconductor*, R. K. Singhal et al., Journal of Physics: Conference Series 200, 062029 (2010)

[40] *Comparative study of ZnO layers prepared by PLD from different targets at various oxygen pressure levels*, D. Hasko et al., Cent. Eur. J. Phys. 7(2) (2009)

[41] *The origin of room temperature ferromagnetism in cobalt-doped zinc oxide thin films fabricated by PLD*, J. H. Kim et al., Journal of the European Ceramic Society **24**, 1847-1851 (2004)

[42] *Pulsed laser deposition of epitaxial Al-doped ZnO film on sapphire with GaN buffer layer*, M. Kumar et al., Thin Solid Films **484** (2005)

[43] *Spectroscopic ellipsometry study of optical transitions in $Zn_{1-x}Co_xO$ alloys*, K. J. Kim et al., Applied Physics Letters **81**, no. 8 (2002)

[44] *Recent progress in processing and properties of ZnO*, S.J. Pearton et al., Progress in Material Science **50**, 293-340 (2005)

[45] *Photoluminescence of a ZnO/GaN Heterostructure Interface*, S.J. Liu et al., Chin. Phys. Lett. **26**/7 077805 (2009)

[46] *Investigation on p-contacts in Mg-doped GaN and the effect of various pre-tretments*, F. Karouta et al., COBRA Inter-University Research Institute on Communication Technology

[47] *Activation of Mg-doped P-GaN by using two-step annealing*, Jun-Dar Hwang et al., Applied Surface Science **253** (2007)

[48] *Properties of Mg activation in thermally treated GaN:Mg films*, C. F. Lin et al., Journal of Applied Physics **88**/ 11 (2000)

[49] *Ti/Au n-type Ohmic contacts to bulk ZnO substrates*, H. S. Yang et al., Applied Physics Letters **87**, 212106 (2005)

[50] *Electrical and Structural Properties of TiÕAu Ohmic Contacts to n-ZnO*, H. K. Kim et al., Journal of The Electrochemical Society **148** G114-G117 (2001)

[51] *Al/Au ohmic contact to n-ZnO by dc sputtering*, J.H. Kim et al., Materials Science and Engineering **B** 165, 77-79 (2009)

[52] *Pt-Ga Ohmic contacts to n-ZnO using focused ion beams*, A. Inumpudi et al., Solid-State Electronics 46/10 (2002)

[53] *Gold schottky contacts on n-type ZnO thin films with an Al/Si(1 0 0) substrates*, G. Yuan et al., Journal of Crystal Growth **268**, 169-173 (2004)

[54] *Surface states dominative Au Schottky contact on vertical aligned ZnO nanorod arrays synthesized by low-temperature growth*, K. Cheng et al., New Journal of Physics **9**, 214 (2007)

[55] *Mean barrier height of Pd Schottky contacts on ZnO thin films*, H. von Wenckstern et al., Applied Physics Letters **88**, 092102 (2006)

[56] *Influence of oxygen vacancies on Schottky contacts to ZnO*, M. W. Allen et al., Applied Physics Letters **92**, 122110 (2008)

[57] *Effect of hydrogen peroxide treatment on the characteristics of Pt Schottky contact on n-type ZnO*, S. H. Kim et al., Applied Physics Letters **86**, 112101 (2005)

[58] *https://www.ntnu.no/wiki/display/nanolab/Rapid+Thermal +Process+Unit+%28RTP%29*, Downloaded 090211

[59] *Pulsed laser deposition of zinc oxide*, Y. Y. Villanueva et al., Thin Solid Films **501**, 366 - 369 (2006)

[60] *Photovoltaic Characterization Laboratory*, Eirik Timo Bøe Vilpponen, Project Thesis at NTNU (2010)

[61] *Semiconductor Measurements and Instrumentation*, W. R. Runyan, Texas Instruments Incorporated (1975)

[62] *Lack of ferromagnetism in n-type cobalt-doped ZnO epitaxial thin films*, T. C. Kaspar et al., New Journal of Physics **10**, 055010 (2008)

[63] *Properties of Mn- and Co-doped bulk ZnO crystals*, A. Y. Polyakov et al., Journal of Vacuum Science Technology **B**, 23/1 (2005)

[64] *Magnetoresistance of Co-doped ZnO thin films*, P. Stamenov et al., Journal of Applied Physics **99**, 08M124 (2006)

[65] *Handbook of X-ray Photoelectron Spectroscopy*, Perkin-Elmer Corporation, Physical Electronics Division (1992)

[66] *Electrical characteristics of Pt Schottky contacts on sulfide-treated n-type ZnO*, S. H. Kim et al., Applied Physics Letters **86**, 022101 (2005)